Hybrid architecture for engineering magnonic quantum networks

C. C. Rusconi,[1,2,3] M. J. A. Schuetz,[4] J. Gieseler,[4] M. D. Lukin,[4] and O. Romero-Isart[1,2]

[1]*Institute for Quantum Optics and Quantum Information of the Austrian Academy of Sciences, A-6020 Innsbruck, Austria*

[2]*Institute for Theoretical Physics, University of Innsbruck, A-6020 Innsbruck, Austria*

[3]*Max-Planck-Institut für Quantenoptik, Hans-Kopfermann-Strasse 1, 85748 Garching, Germany*

[4]*Physics Department, Harvard University, Cambridge, Massachusetts 02318, USA*

(Received 26 September 2018; revised manuscript received 29 July 2019; published 30 August 2019)

We show theoretically that a network of superconducting loops and magnetic particles can be used to implement magnonic crystals with tunable magnonic band structures. In our approach, the loops mediate interactions between the particles and allow magnetic excitations to tunnel over long distances. As a result, different arrangements of loops and particles allow one to engineer the band structure for the magnonic excitations. Furthermore, we show how magnons in such crystals can serve as a quantum bus for long-distance magnetic coupling of spin qubits. The qubits are coupled to the magnets in the network by their local magnetic-dipole interaction and provide an integrated way to measure the state of the magnonic quantum network.

DOI: 10.1103/PhysRevA.100.022343

I. INTRODUCTION

Complex microscopic interactions between particles inside materials often give rise to emergent collective excitations. This collective behavior can be effectively described in terms of weakly interacting quasiparticles that propagate freely in the surrounding medium and follow dispersion relations that are determined by the microscopic details [1]. This treatment allows us to greatly simplify the description of otherwise intractable problems [2]. In many cases, the dispersion relation of quasiparticles can be tailored by a careful design of the host medium. For example, photonic crystals [3] are engineered materials where the propagation of photons is artificially designed by periodically arranging materials with different refractive indices [4]. Quantum emitters can then be coupled to such structures for a variety of applications ranging from quantum simulation [5–8] and quantum information processing [9–11] to the study of open quantum systems [12,13].

Magnons, collective excitations of magnetization in magnetically ordered materials, have recently attracted significant attention in the context of quantum information science. Strong quantum coherent coupling of magnons to a microwave resonator [14–20], optical photons [21–23], and superconducting qubits [24,25] have recently been reported. Magnonic systems [26–28] with tailored magnonic propagation properties are also investigated as a magnon quantum bus to couple quantum emitters over long distances [29–31]. In present magnonic systems, spin-wave propagation between the ferromagnetic elements is mediated by dipolar coupling. Thus, sufficiently high coupling over long distances requires ferromagnets with high saturation magnetization. However, those materials suffer from high losses [32–34]. In contrast, materials such as YIG have little loss but also have a small saturation magnetization and thus a lower magnetic dipole coupling.

In this article, we propose a network of superconducting loops [35] that couples magnetic particles over distances larger than what can be achieved with magnetic dipole-dipole interactions in free space. This allows us to combine low loss materials such as YIG with the desired long-range coupling. In such a setup, the excitation of the collective magnetization in a particle tunnels to other particles provided that there is a superconducting loop between them. This provides a lot of flexibility in the topology of the networks that can be realized with this architecture thereby enabling a wide range of applications. First we describe how to engineer artificial magnonic crystals using a periodic arrangement of magnetic particles and superconducting loops called hereafter a hybrid magnetic lattice (HML), as shown in Fig. 1(a). Second, we discuss how to interface spin qubits with HMLs via their dipolar coupling to the magnetic particles. The coupling enables long-range magnetic coupling of spin qubits and it introduces quantum nonlinear elements into the magnonic crystal. In this context, our proposal offers an *all-magnetic* solid-state alternative to optical quantum emitters coupled to photonic crystals [4]. In addition, the tunability of the magnonic band-gap by an externally applied magnetic field offers a handle that has no analog in photonic systems. Through this feature, the qubit frequency can be tuned to lie inside or outside the band gap, making the qubit dynamics predominantly conservative or dissipative, respectively [4]. Importantly, the band gap can be tuned *on-demand* in real time, thereby giving direct access to various, very different many-body problems simply by varying the external magnetic bias field.

The article is structured as follows. In Sec. II, we discuss how magnonic crystals with a tailored band structure can be designed from a hybrid lattice of superconducting loops and magnetic particles. We first introduce the Hamiltonian describing tunneling of magnons between different magnetic particles via a loop-mediated interaction. Then, we present some specific examples of HMLs. In Sec. III, we discuss in detail the coupling between a qubit and a magnetic particle, and we show how to couple two distant spin qubits via the

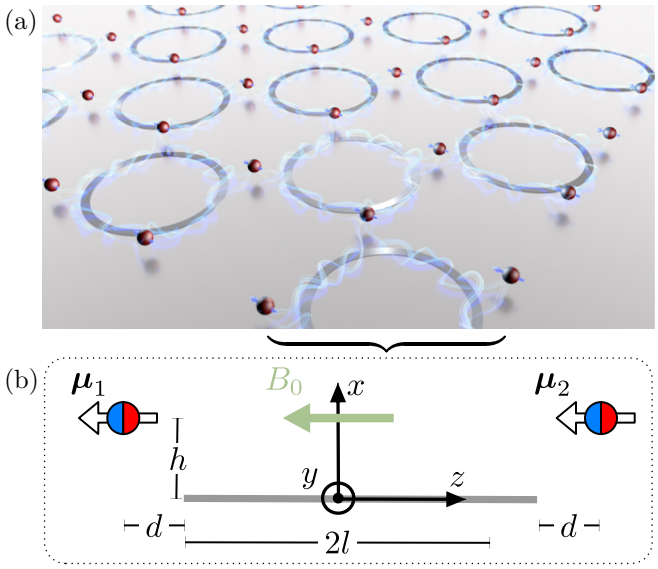

FIG. 1. (a) Schematic illustration of a general hybrid magnetic lattice (HML) of superconducting loops and magnetic particles. (b) Scheme of the simplest cell of the HML: two magnetic particles positioned at a distance d and height h from two opposite points of a superconducting ring of radius l.

HML. Finally, we draw our conclusions in Sec. IV. Further details are provided in the Appendixes.

II. ARTIFICIAL MAGNONIC CRYSTAL

In this section, we focus on how to engineer an HML by placing magnetic particles near superconducting loops. In Sec. II A, we present the Hamiltonian describing the interaction between a single superconducting loop and several magnetic particles. In Sec. II B, we generalize the Hamiltonian to many loops and use this model to discuss specific HML examples.

A. Hamiltonian of the elementary cell: One superconducting loop and several magnets

We consider N magnetic particles with magnetic moments $\boldsymbol{\mu}_j$ $(j = 1, \ldots, N)$ located at positions $\mathbf{r}_j$ near a superconducting circular loop with radius l. An external bias field $\mathbf{B}_0 \equiv -B_0\mathbf{e}_z$ is applied parallel to the plane containing the loop [see the illustration for $N = 2$ in Fig. 1(b)]. We model the superconductive ring as a single-mode LC-resonator, whose self-inductance L and capacitance C are of geometrical origin (see Appendix A). We model the magnetic particle as a sphere of radius R, whose center-of-mass position $\mathbf{r}_j$ lies outside the area encircled by the loop. The applied field $\mathbf{B}_0$ polarizes the magnetic particles uniformly. Therefore, the magnetic field produced by the particles can be approximated as the field generated by a constant magnetic point dipole of magnitude $\mu_j = |\boldsymbol{\mu}_j|$. The coherent dynamics of the system is modeled by the following quantum-mechanical Hamiltonian (see Appendix B for a derivation):

$$\hat{H} = \frac{\hat{Q}^2}{2C} + \frac{1}{2L}\left[\hat{\Phi} - \sum_j \Phi_j(\hat{\boldsymbol{\mu}}_j)\right]^2 - \sum_j \hat{\boldsymbol{\mu}}_j \cdot \mathbf{B}_0 + \frac{1}{2L}\left[\sum_{j=1}^{N} \Phi_j(\hat{\boldsymbol{\mu}}_j)\right]^2 + U_{\mathrm{d}}(\{\hat{\boldsymbol{\mu}}_j\}) + \sum_j \hat{V}_a^j(\hat{\boldsymbol{\mu}}_j). \quad (1)$$

Here, $\hat{Q}$ ($\hat{\Phi}$) is the charge (flux) operator of the loop [36], and

$$\Phi_j(\hat{\boldsymbol{\mu}}_j) \equiv \Phi_{\mathrm{bias}}^j \mathbb{1} + \delta\Phi_j(\Delta\hat{\boldsymbol{\mu}}_j) \quad (2)$$

is the external flux induced in the coil by the magnetic dipole moment $\hat{\boldsymbol{\mu}}_j$. In Eq. (2), Φ_{bias}^j is the field induced in the loop by the magnetic moment at its equilibrium value $\langle\hat{\boldsymbol{\mu}}_j\rangle_0$, while $\delta\Phi_j(\Delta\hat{\boldsymbol{\mu}}_j)$ is the flux induced in the loop by the magnetic moment fluctuation $\Delta\hat{\boldsymbol{\mu}}_j \equiv \hat{\boldsymbol{\mu}}_j - \langle\hat{\boldsymbol{\mu}}_j\rangle_0$. The first two terms in Eq. (1) represent the energy of the loop in the presence of the magnets. The third term refers to the Larmor precession of the magnetic moments about the direction of $\mathbf{B}_0$. The fourth term, $[\sum_j \Phi_j(\hat{\boldsymbol{\mu}}_j)]^2/2L$, represents the total loop-mediated magnetic interaction between the magnets. The magnetic dipole interaction between the magnets, obtained after tracing out all the electromagnetic field modes, is modified (as compared to free space) due to the presence of the loop, which is treated as a single electromagnetic field mode (see Appendix A). The correction to the free dipole-dipole interaction is precisely the fourth term in Eq. (1). The seemingly additional dipole-dipole interaction included in the second term of Eq. (1) is canceled out perfectly when tracing out the loop's electromagnetic field mode (see Appendix B for a detailed derivation). This subtle point was previously discussed in the literature in [37]. The remaining contribution to the magnetic dipole-dipole interaction is mediated by the free-space electromagnetic modes and is represented by $U_{\mathrm{d}}(\{\hat{\boldsymbol{\mu}}_j\})$ in Eq. (1). The last term in Eq. (1) is the magnetic anisotropy energy of each particle, which represents the energy cost of magnetizing the particle along a certain direction due to the interaction between its magnetic moment and its internal crystal structure [38].

Let us now introduce the macrospin $\hat{\mathbf{F}}$ of a magnetic particle, which is related to the magnetic moment by the gyromagnetic relation $\hat{\boldsymbol{\mu}}_j = \hbar\gamma_0\hat{\mathbf{F}}_j$ [39]. In the following, we assume the magnetic particles to be identical, i.e., they have the same gyromagnetic ratio γ_0, the same radius R, and thus the same total spin $\hat{\mathbf{F}}^2 = F(F+1)\mathbb{1}$, where we define $F \equiv \mu/(\hbar\gamma_0)$ and $\mu_j \equiv \mu\,\forall j$. The flux fluctuations in Eq. (2) can be written as $\delta\Phi_j(\Delta\hat{\boldsymbol{\mu}}_j) = \Phi_{\mathrm{e}j}\sum_\nu I_j^\nu \Delta\hat{F}_j^\nu$ $(\nu = x, y, z)$, where $\Delta\hat{\mathbf{F}}_j \equiv \Delta\hat{\boldsymbol{\mu}}_j/(\hbar\gamma_0)$, $\Phi_{\mathrm{e}j} \equiv \hbar\gamma_0\mu_0/4\pi d_j$. Here, d_j is the smallest distance, in the plane containing the loop, between the dipole's position and a point in the loop [see Fig. 1(b)]. I_j^ν is a dimensionless geometrical factor that contains the dependence on the center-of-mass position of the nanomagnet and on the orientation of its magnetic moment (see Appendix C).

For a sufficiently large B_0, such that the thermal energy is negligible compared to the interaction $-\hat{\boldsymbol{\mu}}_j \cdot \mathbf{B}_0$, the fluctuations of the magnetic moment $\Delta\hat{\boldsymbol{\mu}}_j$ can be expressed within the Holstein-Primakoff approximation as $\Delta\hat{\mu}_j^z = \hbar\gamma_0\hat{f}_j^\dagger\hat{f}_j$, $\Delta\hat{\mu}_j^x = \hbar\gamma_0\sqrt{2F}(\hat{f}_j^\dagger + \hat{f}_j)/2$, and

$\Delta\hat{\mu}_j^y = \hbar\gamma_0\sqrt{2F}(\hat{f}_j^\dagger - \hat{f}_j)/(2\mathrm{i})$. The operator $\hat{f}_j$ ($\hat{f}_j^\dagger$) creates (annihilates) an excitation in the uniformly precessing (Kittel) magnonic mode of the jth magnet, and satisfies $[\hat{f}_i, \hat{f}_j^\dagger] = \delta_{ij}$. Within the Holstein-Primakoff approximation (valid when $\langle\hat{f}_j^\dagger\hat{f}_j\rangle \ll 2F$) and the assumption that the LC-circuit is far detuned from the magnonic modes (such that the degrees of freedom of the circuit can be traced out), the coherent dynamics of the magnets reduce to

$$\hat{H}_\mathrm{M} = \hbar\sum_{j=1}^{N}\omega_j\hat{f}_j^\dagger\hat{f}_j + \hbar\sum_{j\neq i=1}^{N}\left(\mathcal{J}_{ij} + \mathcal{J}_{ij}^\mathrm{d}\right)\hat{f}_i^\dagger\hat{f}_j + \hat{V}_\mathrm{lin}. \quad (3)$$

Counter-rotating terms (of the form $\hat{f}_i^\dagger\hat{f}_j^\dagger + \hat{f}_i\hat{f}_j$) have been neglected within the rotating-wave approximation (see Appendix D). Here, $\hat{V}_\mathrm{lin}$ is a linear term in the bosonic operators that can be reabsorbed by defining a new equilibrium position $\langle\hat{\mathbf{F}}\rangle_0$. Notably, for the particular case of the magnetic particles lying in the plane containing the loops, one finds that $\Phi_\mathrm{bias}^j = 0\,\forall j$ and $\hat{V}_\mathrm{lin}$ disappears (see Appendix D). It is thus always possible to write the quadratic Hamiltonian describing the magnon dynamics in a HML as

$$\hat{H}_\mathrm{M} = \hbar\sum_{j=1}^{N}\omega_j\hat{f}_j^\dagger\hat{f}_j + \hbar\sum_{j\neq i=1}^{N}\left(\mathcal{J}_{ij} + \mathcal{J}_{ij}^\mathrm{d}\right)\hat{f}_i^\dagger\hat{f}_j. \quad (4)$$

Here, ω_j is the sum of the frequency associated with the magnetic anisotropy and the Larmor precession frequency due to the total magnetic field, which consists of the external field $\mathbf{B}_0$, the field created by other magnets, and the field created by the superconducting loop (see Appendix D). The second term in Eq. (4) describes magnon tunneling between magnets. The total tunneling rate has two contributions. The contribution from the free-space magnetic dipole-dipole interaction is given by $\mathcal{J}_{ij}^\mathrm{d} \equiv -\hbar\gamma_0^2\mu_0 F(3\sin^2\theta_{ij} - 2)/(8\pi r_{ij}^3)$, where $r_{ij} \equiv |\mathbf{r}_i - \mathbf{r}_j|$ and θ_{ij} is the angle between $\mathbf{r}_i - \mathbf{r}_j$ and $\mathbf{e}_z$. The contribution from the loop-mediated magnetic interaction is given by (see Appendix D)

$$\mathcal{J}_{ij} \equiv \left(\frac{\hbar\gamma_0\mu_0}{4\pi}\right)^2\frac{I_{ij}}{2\hbar d_i d_j L}F. \quad (5)$$

Here, $I_{ij} \equiv I_i^* I_j$, where $I_j \equiv I_j^x + iI_j^y$, depends on the mutual position of the magnetic particles at the sites i, j and on the orientation of their magnetic moments (see Appendix C). In particular, $\mathcal{J}_{ij}$ can be made independent of i, j for symmetric arrangements of magnetic particles around the loop such that $I_{ij} \equiv I$ and $d_j = d\ \forall j$ (see Sec. II B). We stress that $\mathcal{J}_{ij}$ scales as $1/(d_i d_j l)$, where the factor $1/(d_i d_j)$ arises from the $1/d_j$-dependence of $\Phi_j(\hat{\boldsymbol{\mu}}_j)$ and the factor $1/l$ arises from the linear dependence of L on the loop radius [see Eq. (A1)]. For fixed $d_i, d_j \ll l$, the loop-mediated interaction thus leads to a magnon tunneling rate that scales as $\sim 1/r_{ij}$. The minimal possible distance d (and thus the maximum achievable tunneling rate for a given loop geometry) is ultimately set by the critical field tolerated by the loop's wire in the Meissner state (see Appendix E).

As an example, let us consider the simple configuration of one loop and two magnetic particles illustrated in Fig. 1(b) for the particular case of $h = 0$. For this case, one has $\omega_j = 2\gamma_0 k_a/M_\mathrm{s} + \gamma_0 B_0 + \mathcal{J}_{jj} - \hbar\gamma_0^2\mu_0 F/[16\pi(l+d)^3]$, $r_{12} = 2(l+d)$, $\theta_{12} = 0$, and $\mathcal{J}_{12} = [\hbar\gamma_0\mu_0/(4\pi d)]^2 IF/(2\hbar L)$, where $I_{12} = I_{21} \equiv I$. The geometrical inductance of a circular coil is approximated as $L \approx \mu_0 l\ln(8l/\tau)$ for $\tau \ll l$, where τ is the wire thickness. For $l \gg d$, one finds

$$\frac{\mathcal{J}_{12}}{\mathcal{J}_{12}^\mathrm{d}} \approx \frac{(l/d)^2 2I^2}{\pi\ln(8l/\tau)} \gg 1. \quad (6)$$

For $R = 1\ \mu$m, $d = 1.5\ \mu$m, $l = 30\ \mu$m, $h = 0$, and $\tau = 50$ nm, which leads to $I \approx 1.9$ [40], the tunneling rate due to the inductive magnetic interaction is then $\mathcal{J}_{12}/2\pi \approx 5.85$ MHz whereas the one due to the magnetic dipole interaction is $\mathcal{J}_{12}^d/2\pi \approx 0.09$ MHz. In general, for sufficiently large loop size, magnetic dipole-dipole interactions are negligible as compared to loop-mediated coupling [see Fig. 6(b) in Appendix F]. In this case, the magnon tunneling can be approximated by $\mathcal{J}_{ij}$. We remark that larger tunneling rates could be obtained by inscribing the magnets in the contour defined by the loop (see Appendix F). However, this configuration will not be considered further since it is not well suited for building large networks.

B. Examples of hybrid magnetic lattices

Let us now focus on how to build networks by periodic arrangements of superconducting loops and magnetic particles. Equation (1) can be directly generalized to the case of many superconducting loops, thus yielding the general Hamiltonian of a HML. In the following, we neglect the magnetic dipole-dipole coupling ($\mathcal{J}_{ij}^d = 0$) and the flux generated in a coil by next-to-nearest-neighbor magnets as well as by neighboring superconducting coils. Furthermore, within the assumption of identical loops, magnetic particles, and relative positioning of particles and loops, the magnon frequency (tunneling rate) is site-independent, namely $\omega_j \equiv \omega_0\ \forall j$ ($\mathcal{J}_{ij} \equiv \mathcal{J}\ \forall i, j$).

In the following, we consider three different examples of HMLs:

(i) A one-dimensional HML, shown in Fig. 2(a), can be described by

$$\hat{H}_\mathrm{M}^\mathrm{1D} = \hbar\omega_0\sum_j\hat{f}_j^\dagger\hat{f}_j + \hbar\mathcal{J}\sum_j(\hat{f}_j^\dagger\hat{f}_{j+1} + \hat{f}_{j+1}^\dagger\hat{f}_j). \quad (7)$$

This textbook Hamiltonian describes magnon tunneling to nearest neighbors in a one-dimensional (1D) crystal with N lattice sites separated by a distance $a = 2(d+l)$. Assuming periodic boundary conditions, $\hat{H}_\mathrm{M}^\mathrm{1D}$ can be diagonalized in the reciprocal space leading to a magnon dispersion relation $\omega(k) = \omega_0 + 2\mathcal{J}\cos(ka)$, where $k = 2\pi n/(Na)$ ($n \in [N/2, N/2-1]$). In the continuum limit ($N \gg 1$), the magnon propagation is thus restricted to the frequency band $\omega \in [\omega_0 - 2\mathcal{J}, \omega_0 + 2\mathcal{J}]$, which can be tuned in real time by simply modifying the external magnetic field B_0, and hence ω_0. Note that this *in situ* tunability is a characteristic feature of the proposed HMLs in this article.

(ii) A HML where N magnets couple to each other with the same strength can be realized with the circular geometry

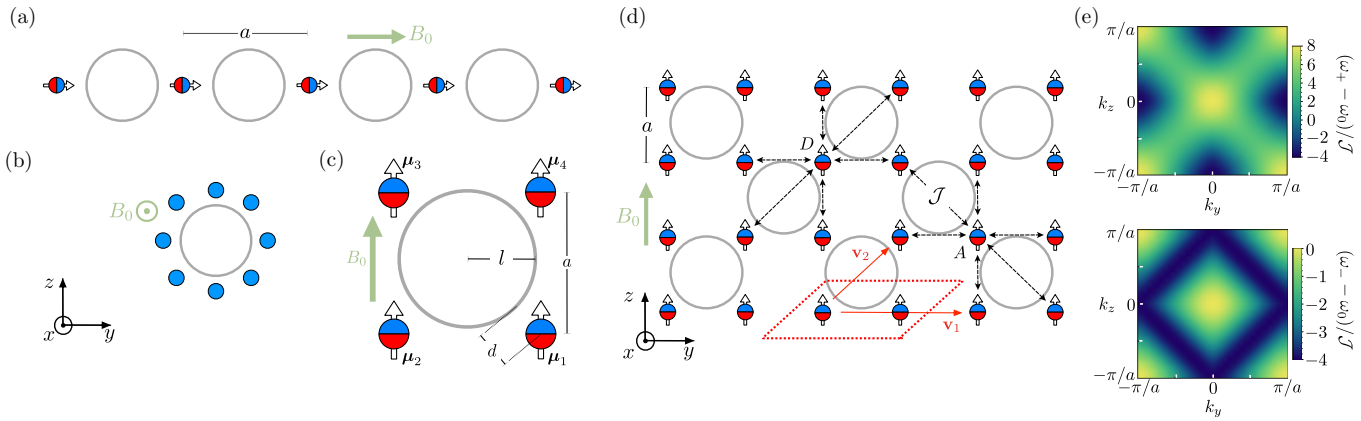

FIG. 2. (a) Top view of a 1D HML. (b) Top view of a system of vertically polarized magnets around a common loop. (c) Unit cell of a 2D HML comprising one loop and four magnetic particles. (d) Top view of a 2D HML implementing a 2D magnonic crystal by a checkerboard arrangement of the single cell in (c). The black dashed arrows indicate coupling between nearest neighbors at the same rate $\mathcal{J}$ and the red dashed area corresponds to the elementary cell of such a magnonic crystal with Bravais vectors $\mathbf{v}_1$ and $\mathbf{v}_2$. (e) Plot for the magnonic bands $(\omega_\pm - \omega_0)/\mathcal{J}$ of the 2D HML in (d).

shown in Fig. 2(b). The Hamiltonian is given by

$$\hat{H}_{\mathrm{M}}^{\mathrm{ND}} = \hbar\omega_0 \sum_{j=1}^{N} \hat{f}_j^\dagger \hat{f}_j + \hbar\mathcal{J} \sum_{i\neq j=1}^{N} \hat{f}_i^\dagger \hat{f}_j, \tag{8}$$

with an all-to-all interaction $\sim\mathcal{J}$ [cf. Eq. (5)]. Here, the geometrical factor $I_{ij} = I$ is different from example (i) due to the fact that the magnets are now polarized perpendicularly to the superconducting coils. In principle, this Hamiltonian could be used to generate magnonic superradiance by enhancing dissipation in the coil and allowing the system to evolve beyond the quadratic approximation [41].

(iii) A two-dimensional HML can be realized by a repetition of the single cell in Fig. 2(c) leading to the structure displayed in Fig. 2(d). Due to the checkerboard arrangements of superconducting loops, we distinguish two magnonic sublattices: magnons in the D (A) sublattice preferably tunnel along the direction of the main diagonal (antidiagonal) in the yz-plane. This HML can thus be described as a 2D Bravais lattice with a basis where each elementary cell contains the two types of sites D and A [see Fig. 2(d)]. The operators $\hat{f}_{\mathbf{j}}^{\mathrm{A}}$, $\hat{f}_{\mathbf{j}}^{\mathrm{A}\dagger}$ ($\hat{f}_{\mathbf{j}}^{\mathrm{D}}$, $\hat{f}_{\mathbf{j}}^{\mathrm{D}\dagger}$), respectively, create and annihilate a magnon in the sublattice A (D) within the cell at position $\mathbf{j} = j_y\mathbf{v}_1 + j_z\mathbf{v}_2 \equiv (j_y, j_z)$, $(j_y, j_z \in \mathbb{Z})$, where $\mathbf{v}_1 = (2a, 0)$ and $\mathbf{v}_2 = (a, a)$ are Bravais vectors. The Hamiltonian of this 2D HML is given by (see Appendix G)

$$\begin{aligned}\hat{H}_{\mathrm{M}}^{\mathrm{2D}} = {} & \hbar\omega_0 \sum_{\mathbf{j}} \left(\hat{f}_{\mathbf{j}}^{\mathrm{D}\dagger}\hat{f}_{\mathbf{j}}^{\mathrm{D}} + \hat{f}_{\mathbf{j}}^{\mathrm{A}\dagger}\hat{f}_{\mathbf{j}}^{\mathrm{A}}\right) \\ & + \hbar\mathcal{J}\left[\sum_{\mathbf{j},\boldsymbol{\beta}} \hat{f}_{\mathbf{j}}^{\mathrm{D}\dagger}\hat{f}_{\mathbf{j}+\boldsymbol{\beta}}^{\mathrm{A}} + \sum_{\mathbf{j},\boldsymbol{\alpha}} \hat{f}_{\mathbf{j}}^{\mathrm{A}\dagger}\hat{f}_{\mathbf{j}+\boldsymbol{\alpha}}^{\mathrm{A}}\right. \\ & \left. + \sum_{\mathbf{j},\boldsymbol{\delta}} \hat{f}_{\mathbf{j}}^{\mathrm{D}\dagger}\hat{f}_{\mathbf{j}+\boldsymbol{\delta}}^{\mathrm{D}} + \mathrm{H.c.}\right].\end{aligned} \tag{9}$$

Here, $\boldsymbol{\beta} \in \{(\pm 1/2, \mp 1), (\pm 1/2, 0)\}$, $\boldsymbol{\alpha} \in \{(\mp 1, \pm 1)\}$, and $\boldsymbol{\delta} \in \{(\pm 1, 0)\}$, with $\boldsymbol{\alpha}$ ($\boldsymbol{\delta}$) and $\boldsymbol{\beta}$ connecting the nearest neighbors of a point along the main antidiagonal (diagonal) and along the z, y direction in the basis specified by $\mathbf{v}_1$ and $\mathbf{v}_2$ [Fig. 2(d)]. The magnon dispersion relation of Eq. (9) leads to two bands given by $\omega_\pm(\mathbf{k}) = \omega_0 + 2\mathcal{J}[4\cos(k_x a)\cos(k_y a) \pm \sqrt{\Lambda}]$, where $\Lambda \equiv 4 + 4\cos(k_x a)\cos(k_y a) - \cos(2k_y a) - \cos(k_x a) + 2\cos(2k_x a)\cos(2k_y a)$, with $a = \sqrt{2}(l + d)$. As shown in Fig. 2(e), the upper band $\omega_+(\mathbf{k})$ features saddle points at $\mathbf{k} = (\pm\pi/2a, \pm\pi/2a)$ where the density of states diverges [42]. As recently shown in [43], these types of exceptional points may give rise to very exotic features in the quantum dynamics of emitters coupled to a two-dimensional crystal.

III. SPIN QUBITS INTERFACED WITH A HYBRID MAGNETIC LATTICE

Our three examples show that HMLs can be engineered to realize artificial long-range magnonic crystals. Let us now address how to magnetically interface spin qubits with the magnons in a given HML. In Sec. III A, we describe the local coupling between a spin qubit and a magnetic particle in a single site of a HML. In Sec. III B, we discuss the sources of dissipation of the system. In Sec. III C, we analyze the magnon-mediated qubit-qubit interaction.

A. Magnon-qubit coupling at a single site

A spin qubit is coupled to a magnetic particle in a HML by local magnetic dipole-dipole interactions. Specifically, we consider the interaction between the jth magnet and an NV-center spin qubit, which is obtained from the $\{|0\rangle, |-1\rangle\}$ subspace of the NV ground-state triplet [44], placed at a position $\mathbf{r}_q$ with respect to the center of the magnet. The Hamiltonian of this system is given by

$$\hat{H}_{\mathrm{MQ}}^{(j)} = \frac{\hbar}{2}\omega_{\mathrm{q}}\hat{\sigma}_j^z - \frac{\hbar}{2}\gamma_q\hat{\boldsymbol{\sigma}}_j \cdot \mathbf{B}(\mathbf{r}_q, \hat{\boldsymbol{\mu}}_j), \tag{10}$$

where $\omega_{\mathrm{q}} \equiv \Delta_{\mathrm{NV}} - \gamma_q B_0$, γ_q is the qubit gyromagnetic ratio (generally different from γ_0), Δ_{NV} is the NV-center zero-field

splitting, and $\mathbf{B}(\mathbf{r}_q, \hat{\boldsymbol{\mu}}_j)$ is the magnetic field generated by the magnet at the position of the qubit. Within the Holstein-Primakoff approximation, the rotating-wave approximation, and assuming the qubit to be positioned along the x-axis of a reference frame centered in the magnet, $\mathbf{r}_q = r_q \mathbf{e}_x$, and oriented as in Fig. 1(b) (see Appendix H for the generalization to any other position), Eq. (10) is approximated by the Jaynes-Cumming Hamiltonian (see Appendix H)

$$\hat{H}^{(j)}_{\mathrm{MQ}} = \tfrac{1}{2}\hbar\omega_{\sigma j}\hat{\sigma}^z_j - \hbar g(\hat{f}^\dagger_j \hat{\sigma}^-_j + \mathrm{H.c.}). \tag{11}$$

Here, $g \equiv 3\hbar\gamma_0\gamma_q\mu_0\sqrt{2F}/(8\pi r_q^3)$ and the qubit frequency $\omega_{\sigma j} = \omega_{\mathrm{q}} + \hbar\gamma_0\gamma_q\mu_0 F/(4\pi r_q^3)$ already contains the shift introduced by the dipole interaction. The dynamics of a general 2D HML with magnetically coupled spin qubits at each lattice site is described by the Jaynes-Cummings-Hubbard Hamiltonian $\hat{H}_{\mathrm{T}} = \hat{H}_{\mathrm{M}} + \sum_{\mathbf{j}} \hat{H}^{(\mathbf{j})}_{\mathrm{MQ}}$, namely in k-space [see Eq. (H14) for the expression in real space]

$$\hat{H}_{\mathrm{T}} = \hbar \sum_{\nu,\mathbf{k}} \omega_\nu(\mathbf{k}) \hat{f}^\dagger_{\nu\mathbf{k}} \hat{f}_{\nu\mathbf{k}} + \hbar \sum_{\mathbf{j}} \frac{\omega_\sigma}{2} \hat{\sigma}^z_{\mathbf{j}} - \hbar \sum_{\nu,\mathbf{j},\mathbf{k}} (g_{\nu\mathbf{j}\mathbf{k}} \hat{f}^\dagger_{\nu\mathbf{k}} \hat{\sigma}^-_{\mathbf{j}} + \mathrm{H.c.}). \tag{12}$$

Here, we introduced the k-space magnonic operator $\hat{f}_{\nu\mathbf{k}} = (1/N)\sum_{\mathbf{j}} \hat{f}_{\nu\mathbf{j}} \exp(-ia\mathbf{j}\cdot\mathbf{k})$, which creates a magnon of momentum $\mathbf{k}$ in the ν-magnonic band propagating in an $N \times N$ 2D lattice characterized by the dispersion relation $\omega_\nu(\mathbf{k})$, and the coupling rate $g_{\nu\mathbf{j}\mathbf{k}} \equiv (g_\nu/N)\exp(-ia\mathbf{j}\cdot\mathbf{k})$, where g_ν is the local coupling to a magnon in the ν-band, a is the HML lattice constant, and $\mathbf{j}$ labels the sites in a 2D HML. In Eq. (12), we neglected the small interaction between the qubit and the loop as well as counter-rotating terms of the form $\hat{\sigma}^+_{\mathbf{j}}\hat{f}^\dagger_{\nu\mathbf{k}} + \hat{\sigma}^-_{\mathbf{j}}\hat{f}_{\nu\mathbf{k}}$ within the rotating-wave approximation, valid provided g, $|\omega_\nu(\mathbf{k}) - \omega_\sigma| \ll \omega_\nu(\mathbf{k})$.

B. Sources of dissipation

The Hamiltonian Eq. (12) can lead to strongly correlated, coherent magnon physics [45,46], provided that the relevant decoherence rates are sufficiently small compared to the coherent coupling rates of the system. While the coherent magnon tunneling $\mathcal{J}$ can reach several MHz (as discussed above), the coherent magnon-qubit coupling can be quantified as $g/(2\pi) \approx 5.2 \times 10^2 (R\ [\mathrm{nm}]^{1/2}/r_q\ [\mathrm{nm}])^3$ MHz, as a function of both the magnet size R and magnet-qubit distance $r_q > R$; see the caption of Fig. 3 for the remaining parameters. The main sources of decoherence arise from qubit dephasing and magnon decay, as any potential damping in the superconducting loop is suppressed by its large detuning. For a NV-center spin qubit, characteristic dephasing times $T_2^* \approx 200\ \mu$s have been reported [47], which can further be increased by dynamical decoupling schemes up to $T_2 \approx 0.5$ s [48]. In the low-temperature regime $\sim$1 K the magnon linewidth [49] for a millimeter-size pure single-crystal YIG sphere has been measured as $\kappa/2\pi \approx 0.5$ MHz [15], at a relatively high magnon frequency of $\sim$10 GHz; this number could potentially be further reduced by working at lower frequencies according to the linear frequency dependence of the Gilbert damping rate in YIG [50]. Accordingly, the regime $\mathcal{J} > \pi/T_2^*, \kappa$ is within reach for particles of size $R \approx 1\ \mu$m (see Sec. II A)

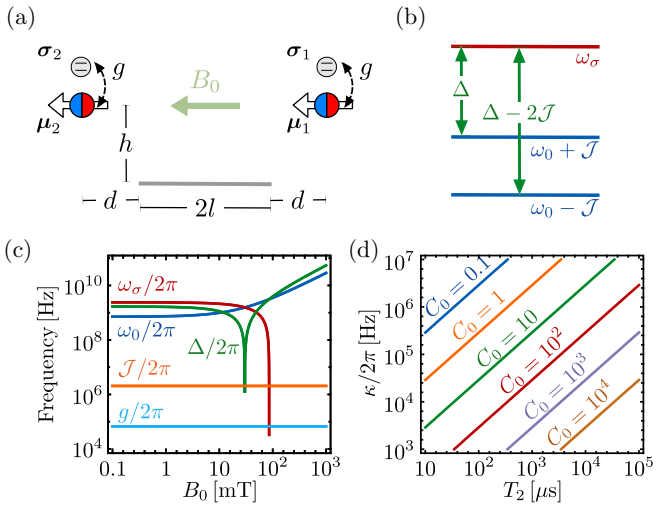

FIG. 3. (a) Elementary HML configuration (single cell) with two identical spin qubits locally coupled to each magnetic particle. (b) Level structure of the system, where $\omega_0 \pm \mathcal{J}$ is the magnonic normal mode of the elementary cell. (c) Relevant frequencies and coupling of the system in (a) as a function of the applied field B_0. (d) Cooperativity C_0 as a function of the decoherence rates κ and π/T_2 for a fixed magnet-qubit coupling g. Other parameters: $R = 350$ nm, $r_q - R = 20$ nm, $d - R = 100$ nm, $l = 5\ \mu$m, $\tau = 50$ nm, $h = 0$, $\gamma_0 = 1.761\,99 \times 10^{11}$ rad Hz T^{-1}, $\gamma_q = 1.761\,49 \times 10^{11}$ rad Hz T^{-1}, $M_s = 196 \times 10^3$ T m^{-3} (YIG saturation magnetization), and $k_a = 2480$ J m^3 (YIG anisotropy energy density). The parameters for YIG are taken from [51].

with current experimental capabilities, while the regime $g > \kappa$ is found to be challenging with the current reported values of the magnon linewidth. However, the detrimental effects due to magnon decay can be reduced efficiently by operating in the dispersive regime, as detailed next.

C. Effective qubit-qubit interaction through a single cell of a HML

Let us consider two identical spin qubits coupled to the elementary configuration described in Fig. 3(a), and thus separated by a distance $2(d + l)$. The system is described by the Hamiltonian $\hat{H}_{\mathrm{T}} = \sum_{j=1}^2 [\hbar\omega_0 \hat{f}^\dagger_j \hat{f}_j + \mathcal{J}\sum_{i\neq j} \hat{f}^\dagger_i \hat{f}_j + \hat{H}^j_{\mathrm{MQ}}]$. In the dispersive regime, when the qubits are detuned from the magnonic eigenmodes of the system, it is possible to adiabatically eliminate the magnonic degrees of freedom. The qubit dynamics are thus described by the following effective spin-spin interaction Hamiltonian (see Appendix I):

$$\hat{H}_{\mathrm{QQ}} = \frac{\hbar}{2}\left[\omega_\sigma - \frac{g^2}{2\Delta} - \frac{g^2}{\Delta - 2\mathcal{J}}\right](\hat{\sigma}^z_1 + \hat{\sigma}^z_2) - \hbar g_{\mathrm{eff}}(\hat{\sigma}^+_1\hat{\sigma}^-_2 + \hat{\sigma}^-_1\hat{\sigma}^+_2), \tag{13}$$

where $\Delta \equiv \omega_0 + \mathcal{J} - \omega_\sigma$, and the effective spin-spin coupling strength reads $g_{\mathrm{eff}} = g^2[1/\Delta - 1/(\Delta - 2\mathcal{J})]$. The level structure and typical values of frequencies and couplings are shown in Figs. 3(b) and 3(c). $\hat{H}_{\mathrm{QQ}}$ can be used to swap excitations between the two qubits at a rate π/g_{eff} whenever $g_{\mathrm{eff}} \gg \gamma, \kappa_{\mathrm{eff}}$, where $\gamma \equiv \pi/T_2^*$ and $\kappa_{\mathrm{eff}} = \kappa g^2[1/\Delta^2 + 1/(\Delta - 2\mathcal{J})^2]$ is the qubit damping induced by the lossy

magnonic bus (see Appendix I) [52]. In this strong-coupling regime, the error ε on the state transfer fidelity for optimized values of the detuning Δ and magnon-tunneling $\mathcal{J}$ is given by $\varepsilon \approx \sqrt{\alpha_\kappa \alpha_\gamma/(2C_0)}$ with cooperativity $C_0 \equiv g^2/(\gamma\kappa)$ where we numerically estimate $\alpha_\gamma \simeq 0.779$ and $\alpha_\kappa \simeq 0.006$ as detailed in Appendix I. In Fig. 3(d), values of C_0 are shown as a function of magnon damping κ and qubit dephasing times T_2 and fixed values for the remaining parameters. As qubit dephasing times $T_2 \approx 0.5$ s are achievable with dynamical decoupling schemes [48], the main limitation is given by the magnon damping rate [15] for the current experimental state of the art.

IV. CONCLUSIONS

In conclusion, we have shown that hybrid magnetic lattices allow us to implement artificial magnonic crystals with engineered band structures. Our approach extends the range of magnetic interactions beyond the limit set by free-space magnetic-dipole interactions and provides an attractive alternative to existing methods, where magnonic crystals are built from arrays of dipolarly coupled nanostripes of magnetic materials [32–34]. Furthermore, it presents an alternative platform to study magnetic crystallization and the dynamics of low-density ensembles of nanomagnets embedded in a nonmagnetic matrix. Thus, it is relevant for the field of artificial spin systems [53,54]. For those systems it would be interesting to replace the lattice of loops with a superconducting wire network [55,56], since this would allow us to study how the interplay between connectivity and superconductivity affects the dynamics of magnetic particles in the network. In addition, spin qubits coupled to the magnets in the network allow us to perform local magnetometry and thereby probe the state of the network. The spin network configuration also allows us to use magnons as a quantum bus to magnetically couple spin qubits over long distances [31], analogously to what is done with quantum emitters coupled to photonic crystals [4], albeit in a different parameter regime.

The potential of our proposal depends very much on the linewidth of magnons in a magnetic sphere. While the microscopic origin of such damping is still not completely understood, interesting strategies to possibly reduce the damping can be envisioned. Smaller magnetic particles might show a lower damping at $T \gtrsim 1$ K due to the discretization of phononic modes in the sample. A levitated version of our proposal [57,58] might allow us to study the impact of the conservation of total angular momentum on the (dissipative) dynamics of the magnetization. Finally, we remark that the present discussion could be generalized beyond the macrospin approximation to include other magnonic modes inside the magnetic particles, which might result in an improvement on the magnon linewidth [59].

ACKNOWLEDGMENTS

We thank J. I. Cirac, D. De Bernardis, J. J. Garcia-Ripoll, G. Kirchmair, K. Lehnert, C. Navau, J. Prat-Camps, P. Rabl, and A. Sanchez for useful discussions. We thank M. Juan for support with graphical illustrations. C.C.R. and O.R.-I. acknowledge support from the European Research Council (ERC-2013-StG 335489 QSuperMag) and the Austrian Federal Ministry of Science, Research, and Economy (BMWFW). M.J.A.S. thanks the Humboldt foundation for financial support. J.G. acknowledges support from the European Union (SEQOO, H2020-MSCA-IF-2014, No. 655369).

C.C.R. and M.J.A.S. contributed equally to this work.

APPENDIX A: DESCRIPTION OF A SUPERCONDUCTING LOOP

In this Appendix, we describe a superconducting loop as a multimode microwave resonator, and we derive under which conditions it can be approximated as a single-mode LC-oscillator.

Superconducting rings on top of a dielectric substrate have been shown to behave as microwave multimode resonators [60,61] characterized by a large quality factor $Q \approx 10^6$ at GHz frequencies [62–64]. The spectrum of the resonator is doubly degenerate, each frequency corresponding to both a clockwise and a counterclockwise traveling wave. Within a transmission line model, the mode frequencies can be approximated by $\omega_n/2\pi \equiv n/(2\pi l\sqrt{L_l C_l})$ for $n \in \mathbb{N}$, where L_l (C_l) is the inductance (capacitance) per unit length of the loop and l is the loop radius.

Adjusting the external magnetic field B_0 so as to tune the Larmor precession frequency of the magnetic particle's macrospin close to the fundamental resonance of the ring resonator, it is possible to neglect the coupling between $\hat{\mathbf{F}}$ and the higher resonant modes. Moreover, the degeneracy of the fundamental mode can be broken by introducing small asymmetries or imperfections, as was done, for instance, in [62,63]. The ring thus behaves as a single-mode LC-resonator of frequency $\omega_c \equiv 1/\sqrt{LC}$, where L (C) is the total inductance (capacitance) of the ring. C is the capacitance between the loop and the ground plate at the opposite end of the dielectric substrate, and it can be arbitrarily reduced by careful design. L amounts to the geometrical self-inductance of the loop, which depends on the particular shape of the loop and on the thickness τ of the wires as detailed in [65]. For the case of a circular loop of radius l and wire of a circular section, the self-inductance reads [65]

$$L = \mu_0 l\left[\ln\left(\frac{8l}{\tau}\right) - \frac{7}{4} + O\left(\frac{\tau^2}{l^2}\right)\right]. \tag{A1}$$

Here we are assuming for simplicity the electric permittivity (magnetic permeability) of the substrate supporting the loop, Fig. 5(a), to be $\varepsilon_r \approx 1$ ($\mu_r \approx 1$).

APPENDIX B: DERIVATION OF THE SYSTEM HAMILTONIAN

In this Appendix, we derive the quantum-mechanical Hamiltonian Eq. (1) describing the dynamics of the coupled system composed by the circuit and the magnetic dipole moments.

Within the single-mode approximation, a superconductive LC-ring resonator can be modeled as an LC-circuit (see Appendix A). The equations of motion for the LC-circuit can be derived from Kirchhoff's current and voltage laws,

together with the constitutive relations, which relate current and voltage at each element of the circuit. Defining $V_C \equiv \partial_t \Phi_C$ ($V_L \equiv \partial_t \Phi_L$) the flux at the capacitor (inductor) of the circuit, we write the constitutive relations for the capacitor as $\ddot{\Phi}_C = I_C/C$ and for the inductor as

$$\Phi_L = L I_L + \sum_{j=1}^{N} \Phi_j(\boldsymbol{\mu}_j). \tag{B1}$$

Here, C (L) are the circuit capacitance (inductance), and $\Phi_j(\boldsymbol{\mu}_j)$ is the flux induced in the ring by the jth magnetic dipole. The equation of motion for the circuit can be derived from Kirchhoff's law as

$$C\ddot{\Phi} + \frac{\Phi}{L} = \sum_{j=1}^{N} \frac{\Phi_j(\boldsymbol{\mu}_j)}{L}, \tag{B2}$$

where $\Phi \equiv \Phi_L = -\Phi_C$ [66].

The coherent dynamics of the magnetic moment $\boldsymbol{\mu}_j \equiv \mu(\cos\varphi_j \sin\theta_j, \sin\varphi_j \sin\theta_j, \cos\theta_j)$, for $\theta_j \in [0, \pi]$ and $\varphi_j \in [0, 2\pi]$, is described by the Landau-Lifshitz equation $\partial_t \boldsymbol{\mu}_j = -\gamma_0 \boldsymbol{\mu}_j \times \mathbf{B}(\mathbf{r}_j)$, where $\mathbf{B}(\mathbf{r}_j)$ is the total magnetic field acting on the jth magnetic moment. In terms of the polar φ_j and azimuthal θ_j angles, the Landau-Lifshitz equations read [67]

$$\dot{\varphi}_j = -\frac{\gamma_0}{\mu \sin\theta_j} \partial_{\varphi_j} U, \quad \dot{\theta}_j = \frac{\gamma_0}{\mu \sin\theta_j} \partial_{\theta_j} U, \tag{B3}$$

where $U \equiv \sum_{j=1}^{N} V_a^j(\boldsymbol{\mu}_j) + U_0 + U_\mathrm{d} + U_\mathrm{ind}$ is the magnetic interaction energy of the dipoles. $V_a^j(\boldsymbol{\mu}_j)$ represents the magnetic anisotropy energy of the jth magnetic particle. $U_0 = -\sum_{j=1}^{N} \boldsymbol{\mu}_j \cdot \mathbf{B}_0$ represents the interaction energy of the dipoles with the external bias field. U_d represents the free-space dipole-dipole interaction energy between the magnetic moments

$$U_\mathrm{d}(\{\boldsymbol{\mu}_j\}) = -\frac{1}{2} \sum_{j=1}^{N} \sum_{i \neq j=1}^{N} \boldsymbol{\mu}_j \cdot \mathbf{B}_i^\mathrm{dip}(\mathbf{r}_j). \tag{B4}$$

The dipolar field created by the dipole moment $\boldsymbol{\mu}_i$ at position $\mathbf{r}$ reads

$$\mathbf{B}_i^\mathrm{dip}(\mathbf{r}) = \frac{\mu_0}{4\pi} \left[\frac{3\Delta\mathbf{r}_i(\boldsymbol{\mu}_i \cdot \Delta\mathbf{r}_i)}{|\Delta\mathbf{r}_i|^5} - \frac{\boldsymbol{\mu}_i}{|\Delta\mathbf{r}_i|^3} \right], \tag{B5}$$

with $\Delta\mathbf{r}_i \equiv \mathbf{r} - \mathbf{r}_i$. $U_\mathrm{ind} = I_L \sum_j \Phi_j(\boldsymbol{\mu}_j)$, where I_L is given by Eq. (B1), represents the interaction between the magnetic dipoles and the field produced by the current flowing in the ring [68].

The equations of motion Eqs. (B2) and (B3) can be derived from the Lagrangian

$$\begin{aligned} \mathcal{L} = {} & \frac{C}{2}\dot{\Phi}^2 + \frac{\mu}{\gamma_0} \sum_{j=1}^{N} \dot{\varphi}_j \cos\theta_j - \frac{1}{2L} \left[\Phi - \sum_{j=1}^{N} \Phi_j(\varphi_j, \theta_j) \right]^2 \\ & - \frac{1}{2L} \left[\sum_{j=1}^{N} \Phi_j(\varphi_j, \theta_j) \right]^2 - \sum_{j=1}^{N} \mu B_0 \cos\theta_j - U_\mathrm{dip} \\ & - \sum_j V_a^j(\varphi_j, \theta_j). \end{aligned} \tag{B6}$$

From Eq. (B6), the classical Hamiltonian of the system is obtained introducing the generalized momenta $Q \equiv C\dot{\Phi}$ and $p_j \equiv \mu \cos\theta_j/\gamma_0$ conjugated to Φ and φ_j, respectively. Following the usual canonical quantization procedure, one can then derive the quantum-mechanical Hamiltonian of the system given in Eq. (1). The charge $\hat{Q}$ and flux $\hat{\Phi}$ operators of the circuit appearing in the system Hamiltonian satisfy canonical commutation relations $[\hat{\Phi}, \hat{Q}] = i\hbar$. The components of the magnetic moment $\hat{\boldsymbol{\mu}}_j \equiv \mu(\sin\hat{\theta}_j \cos\hat{\varphi}_j, \sin\hat{\theta}_j \sin\hat{\varphi}_j, \cos\hat{\theta}_j)^T$ commute as $[\hat{\mu}_j^\nu, \hat{\mu}_i^\eta] = i\mu\delta_{ij}\epsilon_{\nu\eta\xi}\hat{\mu}_j^\xi$ for $\nu, \eta, \xi = x, y, z$, according to the canonical quantization of the classical Poisson bracket,

$$\{f, g\} = -\sum_{j=1}^{N} \frac{1}{\mu \sin\theta_j} \left(\frac{\partial f}{\partial\varphi_j}\frac{\partial g}{\partial\theta_j} - \frac{\partial f}{\partial\theta_j}\frac{\partial g}{\partial\varphi_j} \right), \tag{B7}$$

for any f, g functions of θ_j, φ_j.

APPENDIX C: MAGNETIC FLUX THROUGH A COIL

In this Appendix, we derive the expression for the flux induced by a magnetic dipole moment in a neighboring superconducting loop.

We consider the inductive coupling between a magnet with magnetic moment $\hat{\boldsymbol{\mu}} = \hbar\gamma_0\hat{\mathbf{F}}$ and a coil of arbitrary shape. We assume the magnet to be placed at a distance h above the coil and at a horizontal distance d from the coil's closest wire [see Fig. 1(b) in the main text]. The flux induced in the coil by the magnet reads

$$\Phi(\hat{\mathbf{F}}) = \oint d\mathbf{l} \cdot \mathbf{A}(\mathbf{r}, \hat{\mathbf{F}}), \tag{C1}$$

where $\mathbf{A}(\mathbf{r}, \hat{\mathbf{F}})$ is the magnetic vector potential generated by the magnet, and the integral is taken on the contour defined by the coil. Equation (C1) can be written as $\Phi(\hat{\mathbf{F}}) = \hbar\gamma_0\mu_0 \sum_\nu I_\nu \hat{F}_\nu/(4\pi d)$ for $\nu = x, y, z$, where

$$I_\nu \equiv d \oint \frac{(\Delta\mathbf{r} \times d\mathbf{l})_\nu}{|\Delta\mathbf{r}|^3} \tag{C2}$$

is a dimensionless factor that depends only on the shape of the coil and on the mutual position of the magnet and the coil. Here $\Delta\mathbf{r}$ is the distance between the magnet and a point in the coil. For instance, for a circular coil of radius l centered at $(0, 0, l + d)$ and for a nanomagnet at a position $(h, 0, 0)$, the factors I_ν in Eq. (C2) read

$$\begin{aligned} I_z &= \int_{-l/d}^{l/d} d\lambda\, F\left(\lambda, \frac{l}{d}, \frac{h}{d}\right), \\ I_x &= \int_{-l/d}^{l/d} d\lambda\, G\left(\lambda, \frac{l}{d}, \frac{h}{d}\right), \end{aligned} \tag{C3}$$

and $I_y = 0$, where

$$\begin{aligned} F(\lambda, x, y) &\equiv \frac{y\lambda/\sqrt{x^2 - \lambda^2}}{[y^2 + x^2 + (x+1) + 2\lambda(x+1)]^{3/2}}, \\ G(\lambda, x, y) &\equiv \frac{\sqrt{x^2 - \lambda^2} + \frac{\lambda}{\sqrt{x^2-\lambda^2}}(x + 1 + \lambda)}{[y^2 + x^2 + (x+1) + 2\lambda(x+1)]^{3/2}}. \end{aligned} \tag{C4}$$

As shown in Fig. 4, the integrals in Eq. (C3) have an optimal value around unity as a function of h/d in the limit of a large loop radius, $l/d \gg 1$.

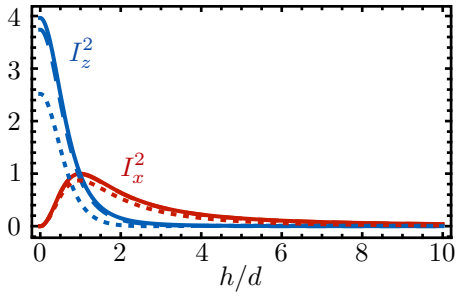

FIG. 4. Plot of the parameters I_z and I_x as a function of h/d for $l/d = 10$ (dotted line), 10^2 (dashed line), and 10^3 (solid line). For I_x the dashed and solid lines are almost coincident.

APPENDIX D: MAGNON DYNAMICS IN A HML: HAMILTONIAN DERIVATION

In this Appendix, starting from Eq. (1), we derive Eq. (4), which describes the propagation of magnons in a HML. We consider the simple case of two magnets as depicted in Fig. 1(b) (generalization to the case of several magnets is straightforward). By substituting the definition Eq. (2) into Eq. (1), one obtains

$$\hat{H} = \hbar\omega_c \hat{a}^\dagger \hat{a} - \frac{\Phi_c}{L}(\hat{a}^\dagger + \hat{a})\delta\hat{\Phi} + \hbar\omega_L \sum_{j=1}^{2} \hat{F}_j^z + \frac{(\delta\hat{\Phi})^2}{L} + \frac{\Phi_{\text{bias}}}{L}\delta\hat{\Phi} + \hat{U}_{\text{d}}(\{\hat{\boldsymbol{\mu}}_j\}) + \sum_{j=1}^{2} \hat{V}_a^j(\hat{\boldsymbol{\mu}}_j), \tag{D1}$$

where $\omega_c \equiv 1/\sqrt{LC}$, $\Phi_{\text{bias}} \equiv \sum_j \Phi_{\text{bias}}^j$, and $\delta\hat{\Phi} \equiv \sum_j \delta\Phi_j(\Delta\hat{\boldsymbol{\mu}}_j)$. Here, we expressed the circuit operators in terms of creation and annihilation operators $(\hat{\Phi} - \Phi_{\text{bias}}) \equiv \Phi_c(\hat{a}^\dagger + \hat{a})$ and $\hat{Q} \equiv i(\hat{a}^\dagger - \hat{a})/(2\Phi_c)$, where $\Phi_c \equiv \sqrt{\hbar/(2C\omega_c)}$.

We consider the applied field $\mathbf{B}_0$ to be sufficiently large so as to initially polarize the macrospin at the two nodes along $-\mathbf{e}_z$, such that $\langle\hat{\mathbf{F}}_j\rangle_0 = -F\mathbf{e}_z$. The fluctuations of $\hat{\mathbf{F}}_j$ around the equilibrium state can be described by a bosonic mode $\hat{f}_j, \hat{f}_j^\dagger$ (magnon) according to the Holstein-Primakoff approximation $\hat{F}_j^z = -F + \hat{f}_j^\dagger \hat{f}_j$ and $\hat{F}_j^+ \simeq \sqrt{2F}\hat{f}_j^\dagger$. In the limit of small fluctuations $\langle\hat{f}_j^\dagger \hat{f}_j\rangle \ll 2F$, $\hat{H}$ can be approximated by a quadratic Hamiltonian in the bosonic operators $\hat{a}^\dagger$, $\hat{a}$, $\hat{f}_j^\dagger$, and $\hat{f}_j$ as

$$\hat{H} \simeq \hbar\omega_c \hat{a}^\dagger \hat{a} - \hbar(\hat{a}^\dagger + \hat{a})\sum_{j=1}^{2}(\chi_j \hat{f}_j + \text{H.c.}) + \hbar\sum_{j=1}^{2}\left\{\omega_j \hat{f}_j^\dagger \hat{f}_j + 2\sum_i(\Lambda_{ij}\hat{f}_i^\dagger \hat{f}_j^\dagger + \text{H.c.}) + \sum_{i,j=1}^{2}\left[(2-\delta_{ij})\mathcal{J}_{ij} + (1-\delta_{ij})\mathcal{J}_{ij}^{\text{d}}\right]\hat{f}_i^\dagger \hat{f}_j\right\} + \hbar\sum_{j=1}^{2}(\eta_j \hat{f}_j + \eta_j^* \hat{f}_j^\dagger). \tag{D2}$$

We have defined

$$\omega_j \equiv \gamma_0 B_0 + 2\frac{\gamma_0 k_a}{M_{\text{s}}} + \mathcal{J}_{jj} + \sum_{i=1}^{2}\frac{\hbar\gamma_0^2\mu_0}{4\pi r_{ij}^3}(3\cos^2\theta_{ij} - 1)F, \tag{D3}$$

$$\Lambda_{ij} \equiv -3(1-\delta_{ij})\frac{\hbar\gamma_0^2\mu_0}{16\pi r_{ij}^3}F\sin^2\theta_{ij}e^{i2\varphi_{ij}} + \frac{\Phi_e^2 F}{2\hbar L}I_j I_i, \tag{D4}$$

$$\mathcal{J}_{ij} \equiv \left(\frac{\hbar\gamma_0\mu_0}{4\pi}\right)^2 \frac{I_{ij}F}{2\hbar d_i d_j L}, \tag{D5}$$

$$\mathcal{J}_{ij}^{\text{d}} \equiv -\frac{\hbar\gamma_0^2\mu_0}{8\pi r_{ij}^3}(3\sin^2\theta_{ij} - 2)F, \tag{D6}$$

$$\chi_j \equiv \frac{\Phi_{\text{e}}\Phi_c}{2\hbar L}I_j\sqrt{2F}, \tag{D7}$$

$$\eta_j \equiv \sum_i \frac{3\hbar\mu_0\gamma_0^2}{8\pi r_{ij}^3}F\sqrt{2F}e^{i2\varphi_{ij}}\cos\theta_{ij}\sin\theta_{ij} + \frac{\Phi_{\text{e}}\Phi_{\text{bias}}}{2\hbar L}\sqrt{2F}I_j. \tag{D8}$$

Here, Φ_e is independent of j as we assumed the particles to be at the same distance d from the loop's wire (see Sec. II A), k_a is the magnetic anisotropy energy density, and M_{s} is the saturation magnetization of the magnetic particle. We additionally assumed the easy magnetization axis of the magnetic anisotropy potential of the material to be aligned along the direction of the applied magnetic field. In this case, the anisotropy energy contributes only as a shift to the magnon oscillation frequency within the quadratic approximation.

The linear term in Eq. (D2) shifts the equilibrium orientation of the magnetic moments and the equilibrium value of the flux in the loop. It can be formally eliminated from Eq. (D2) displacing the bosonic operators $\hat{a}^\dagger$, $\hat{a}$, $\hat{f}_j^\dagger$, and $\hat{f}_j$ to represent the fluctuations around the new equilibrium values. The linear term in Eq. (D2) is identically zero when the magnetic particles are placed in the plane of the LC-resonator ($h = 0$), as in Fig. 5(a), and the distance between the magnets is such that the free-space dipole-dipole interaction is negligible [69]. We thus neglect hereafter the last term in Eq. (D2) assuming the shift in the relevant couplings and frequencies to be negligible ($h \sim 0$). We remark that all the quantitative predictions made in the main text are calculated for $h = 0$ and negligible dipole-dipole interaction.

Due to the large detuning between ω_c and the frequencies defined in Eqs. (D3)–(D7), we adiabatically eliminate the LC-resonator degrees of freedom, which are assumed to be in the vacuum state. Within the rotating-wave approximation and taking into account the circuit-induced shifts of the frequencies and couplings, one obtains the effective Hamiltonian Eq. (4) that describes the magnon dynamics.

APPENDIX E: MAGNETIC FIELD INTENSITY AT THE WIRES OF THE LOOP

Here, we calculate the field produced by the magnetic particle at the wire of the loop. From the requirement that this field should not exceed the critical field to keep the loop in the

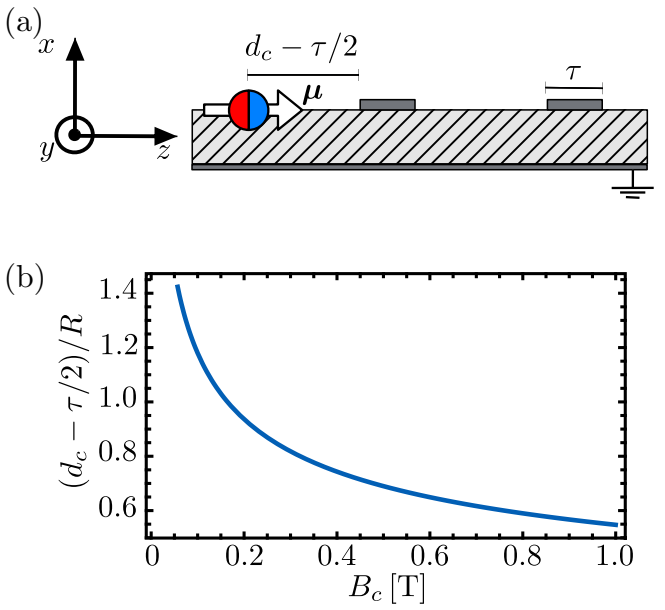

FIG. 5. (a) Lateral view (not to scale) of a magnetic particle positioned on the substrate (hatched gray region) sustaining the superconducting ring ($h = 0$) at a distance $d - \tau/2$ from the closest point of the superconducting-ring wire (dark gray region) of thickness τ. (b) Critical distance $d_c - \tau/2$ in units of R at which the field produced by the magnetic moment at the closest wire point equals B_c. Other physical parameters are taken from the caption of Fig. 3.

Meissner state, we derive the minimal distance from the wire at which a magnetic particle can be placed.

The magnetic field produced by the particle at any point in the wire must be smaller than the critical field (first critical field) B_c of the type I (type II) superconductor that makes up the loop. Consider the situation illustrated in Fig. 5(a). The distance at which the center of the magnetic particle should be placed such that the $\mathbf{e}_z$-component of the magnetic field at the closest point of the loop equals B_c reads

$$d_c = \frac{\tau}{2} + \left(\frac{2\mu_0 M_s}{3B_c}\right)^{1/3} R, \tag{E1}$$

where M_s is the saturation magnetization of the magnetic particle, R is the particle radius, and τ is the wire thickness. In Fig. 5(b), $(d_c - \tau/2)/R$ is plotted as a function of the field B_c at the wire position. For the values used in Fig. 3, the field produced by the magnetic particle at the position of the loop wire is ≈110 mT, which is below the first critical field of many type II superconductors such as Nb [70].

APPENDIX F: BONE-SHAPED CONFIGURATION

In the following, we analyze a different coil geometry in which the magnets are inscribed inside the perimeter defined by the coil's wire. We show that while such a configuration is not suitable to build hybrid magnetic lattices, it can achieve a larger magnon tunneling rate than the configuration in Fig. 1(b). Let us consider the situation illustrated in Fig. 6(a), where two magnets are coupled through a bone-shaped loop. Here, d is the radius of the circular end-rings, w is the separation of the middle parallel wires, and $2l$ is their length.

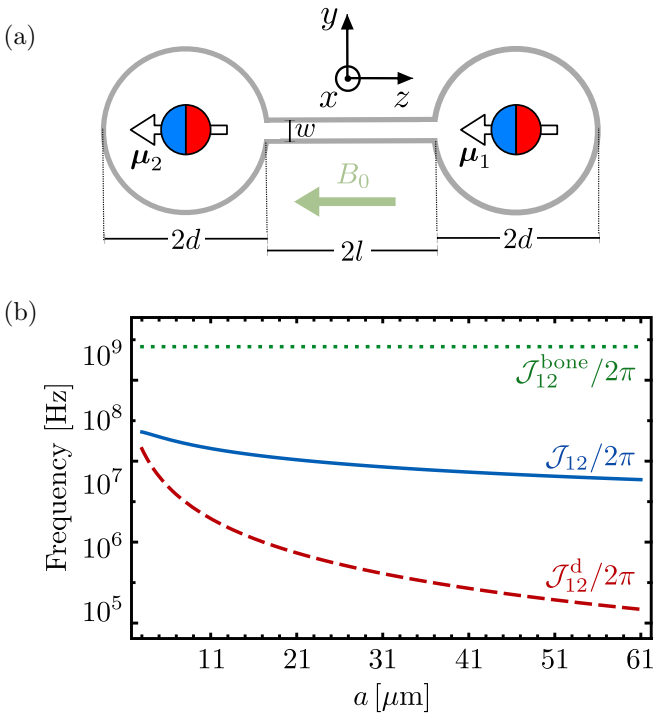

FIG. 6. (a) Bone-shaped coil for enhancing the magnon tunneling rate between distant magnets. In such a configuration the total distance between the magnets is $a = 2d + 2l$. (b) Magnon tunneling rate $\mathcal{J}_{12}$ (solid blue line), $\mathcal{J}_{12}^{\rm d}$ (dashed red line), and $\mathcal{J}_{12}^{\rm bone}$ (dotted green line) as a function of the magnets separation a. We assumed $R = 1$ μm, $d = 500$ nm, and $\tau = 50$ nm. The tunneling rate $\mathcal{J}_{12}$ ($\mathcal{J}_{12}^{\rm d}$) corresponds to the loop-mediated (free-space magnetic dipole) tunneling rate in the configuration shown in Fig. 1(b).

For $w \ll d^2/l$, the middle region connecting the two circular ends of the loop has a negligible contribution to the self-inductance L of the loop. Moreover for $R < d$, the magnetic flux produced by the magnetic particle is obtained as the flux generated by a magnetic moment $\boldsymbol{\mu}$ placed at the origin of a circular coil and of intensity $\mu = M_s 4\pi R^3/3$. For $l \gg d$, the flux produced by a magnet in the loop at the opposite end of the coil can be neglected. The fluctuating magnetic moment $\hat{\boldsymbol{\mu}}_j$ produces a fluctuating flux $\hat{\Phi}_j = \hbar\gamma_0\mu_0\Delta\hat{F}_x/(4l)$, where $\Delta\hat{F}_y$ and $\Delta\hat{F}_z$ contribute only at higher order. In this configuration, the direct inductive magnetic coupling contribution to the magnon-tunneling rate thus reads

$$\mathcal{J}_{12}^{\rm bone} \equiv \frac{\gamma_0^2\mu_0^2\hbar F}{8d^2 L}. \tag{F1}$$

Here, L represents the inductance of a circular coil of radius d [cf. Eq. (A1)].

In Fig. 6(b), $\mathcal{J}_{12}^{\rm bone}$ is plotted as a function of the magnet separation $a = 2(l + d)$, keeping d fixed. Realistically, at larger values of l the contribution of the middle region to the total inductance will affect the scaling of $\mathcal{J}_{12}^{\rm bone}$. However, for a sufficiently small separation w between the two parallel wires, the tunneling rate is expected to vary only slightly with an increase of l. The bone-shaped configuration [Fig. 6(a)] thus allows us to enhance the magnon tunneling rate for a

given separation a as compared to the simpler configuration in Fig. 1(b).

APPENDIX G: HAMILTONIAN FOR THE 2D HML

In this Appendix, we derive the Hamiltonian Eq. (9), which describes the two-dimensional HML illustrated in Fig. 2(d), whose band structure is shown in Fig. 2(e).

Let us consider the elementary cell of such a configuration shown in Fig. 2(c). For large loop size l, $\mathcal{J}_{ij}^{d} \ll \mathcal{J}_{ij}$ [see Fig. 6(b)], and thus the magnon tunneling rate is given by $\mathcal{J}_{ij} = \mathcal{J}\, e^{i\phi_{ij}}$, with

$$\mathcal{J} = \frac{\Phi_e^2 F}{2\hbar L}\left(I_x^2 + I_y^2\right), \tag{G1}$$

where we defined $I_x \equiv I_1^x = I_2^x = I_3^x = I_4^x$ and $I_y \equiv I_1^y = I_3^y = -I_2^y = -I_4^y$, and ϕ_{ij} is a function of I_x, I_y. The magnon dynamics in the elementary cell in Fig. 2(c) is thus described by

$$\hat{H}_{\mathrm{M}}^{\mathrm{cell}} = \hbar\omega_0 \sum_{j=1}^{4} \hat{f}_j^{\dagger}\hat{f}_j + \hbar\mathcal{J} \sum_{i\neq j=1}^{4} \hat{f}_i^{\dagger}\hat{f}_j, \tag{G2}$$

where we redefined some of the magnonic operators to absorb the phase factor appearing in the tunneling rate $\mathcal{J}_{ij}$.

The extended 2D HML shown in Fig. 2(d) is built by repetition of this elementary cell. As discussed in the main text, the magnon dynamics of such a 2D HML can be described by a two-interacting-sublattices model, labeled by A and D according to the Hamiltonian

$$\begin{aligned}\hat{H}_{\mathrm{M}}^{\mathrm{2D}} =& \hbar\omega_0 \sum_{\mathbf{j}} \left(\hat{f}_{\mathbf{j}}^{\mathrm{D}\dagger}\hat{f}_{\mathbf{j}}^{\mathrm{D}} + \hat{f}_{\mathbf{j}}^{\mathrm{A}\dagger}\hat{f}_{\mathbf{j}}^{\mathrm{A}}\right) \\ &+ \hbar\mathcal{J}\left[\sum_{\mathbf{j},\boldsymbol{\beta}} \hat{f}_{\mathbf{j}}^{\mathrm{D}\dagger}\hat{f}_{\mathbf{j}+\boldsymbol{\beta}}^{\mathrm{A}} + \sum_{\mathbf{j},\boldsymbol{\alpha}} \hat{f}_{\mathbf{j}}^{\mathrm{A}\dagger}\hat{f}_{\mathbf{j}+\boldsymbol{\alpha}}^{\mathrm{A}}\right. \\ &\left. + \sum_{\mathbf{j},\boldsymbol{\delta}} \hat{f}_{\mathbf{j}}^{\mathrm{D}\dagger}\hat{f}_{\mathbf{j}+\boldsymbol{\delta}}^{\mathrm{D}} + \mathrm{H.c.}\right].\end{aligned} \tag{G3}$$

Here, the operators $\hat{f}_{\mathbf{j}}^{\mathrm{A}}$, $\hat{f}_{\mathbf{j}}^{\mathrm{A}\dagger}$ ($\hat{f}_{\mathbf{j}}^{\mathrm{D}}$, $\hat{f}_{\mathbf{j}}^{\mathrm{D}\dagger}$) create and annihilate a magnon in the sublattice A (D) within the cell at position $\mathbf{j} = (j_y, j_z)$, and the vectors $\boldsymbol{\alpha}$ and $\boldsymbol{\beta}$ ($\boldsymbol{\delta}$ and $\boldsymbol{\beta}$), for $\boldsymbol{\beta} \in \{(\pm 1/2, \mp 1), (\pm 1/2, 0)\}$, $\boldsymbol{\alpha} \in \{(\mp 1, \pm 1)\}$, and $\boldsymbol{\delta} \in \{(\pm 1, 0)\}$, connect the nearest neighbors of a point in the sublattice A (D) in the basis of the Bravais vectors $\mathbf{v}_1$ and $\mathbf{v}_2$.

In terms of the operators

$$\hat{f}_{\mathbf{k}}^{\mathrm{D}} = \frac{1}{N}\sum_{\mathbf{j}} e^{+i\mathbf{k}\cdot\mathbf{j}}\hat{f}_{\mathbf{j}}^{\mathrm{D}}, \tag{G4}$$

$$\hat{f}_{\mathbf{k}}^{\mathrm{D}\dagger} = \frac{1}{N}\sum_{\mathbf{j}} e^{-i\mathbf{k}\cdot\mathbf{j}}\hat{f}_{\mathbf{j}}^{\mathrm{D}\dagger}, \tag{G5}$$

$$\hat{f}_{\mathbf{k}}^{\mathrm{A}} = \frac{1}{N}\sum_{\mathbf{j}} e^{+i\mathbf{k}\cdot\mathbf{j}}\hat{f}_{\mathbf{j}}^{\mathrm{A}}, \tag{G6}$$

$$\hat{f}_{\mathbf{k}}^{\mathrm{A}\dagger} = \frac{1}{N}\sum_{\mathbf{j}} e^{-i\mathbf{k}\cdot\mathbf{j}}\hat{f}_{\mathbf{j}}^{\mathrm{A}\dagger}, \tag{G7}$$

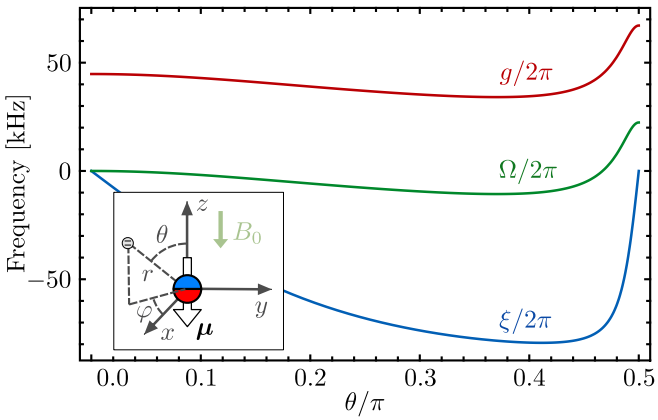

FIG. 7. Plot of the couplings ξ, g, and Ω vs the position angle θ. The remaining parameter have the following values: $R = 350$ nm, $r_0 = R + 20$ nm, $B_0 = 70$ mT, and γ_0, γ_q as in the caption of Fig. 3. Inset: general configuration of the nanomagnet-qubit system.

which create or annihilate a magnon of momentum $\mathbf{k} = (k_y, k_z)$ in the sublattice D or A, the Hamiltonian in Eq. (G3) can be written as $\hat{H}_{\mathrm{M}}^{\mathrm{2D}} = 2\mathcal{J}\hat{\Psi}^{\dagger}M\hat{\Psi}$, where $\hat{\Psi} \equiv (\hat{f}_{\mathbf{k}}^{\mathrm{D}}, \hat{f}_{\mathbf{k}}^{\mathrm{A}})^T$ and

$$M \equiv \begin{pmatrix} 2\cos[(k_y + k_z)a] & \cos(k_y a) + \cos(k_z a) \\ \cos(k_x a) + \cos(k_y a) & 2\cos[(k_x - k_y)a] \end{pmatrix}. \tag{G8}$$

The eigenvalues of $\hat{H}_{\mathrm{M}}^{\mathrm{2D}}$ read

$$\omega_{\pm}(\mathbf{k}) = \omega_0 + 2\mathcal{J}[4\cos(k_x a)\cos(k_y a) \pm \sqrt{\Lambda}], \tag{G9}$$

where $\Lambda \equiv 4 + 4\cos(k_x a)\cos(k_y a) - \cos(2k_y a) - \cos(k_x a) + 2\cos(2k_x a)\cos(2k_y a)$, with $a = \sqrt{2}(l + d)$ being the lattice constant. Equation (G9) corresponds to the magnon bands illustrated in Fig. 2(e).

APPENDIX H: SPIN QUBITS COUPLED TO A HML

In this Appendix, we derive the general Hamiltonian Eq. (12) describing NV-center qubits coupled to the magnetic particles in a HML. In particular, we obtain first Eq. (11) for an NV-center qubit coupled to a magnetic particle by magnetic dipole-dipole interaction, and we later generalize this result to the case of several NV-center qubits coupled to a HML.

Let us first consider a single NV-center located at $\mathbf{r}_q \equiv r_q(\sin\theta\cos\varphi, \sin\theta\sin\varphi, \cos\theta)$ around a magnetic particle (see the inset Fig. 7). The magnetic dipole interaction Hamiltonian between the NV-center and the magnetic particle reads

$$\hat{H}_{\text{M-NV}} = \hbar\Delta_{\mathrm{NV}}\hat{S}_z^2 + \gamma_q B_0 \hat{S}_z - \hbar\gamma_q \hat{\mathbf{S}}\cdot\hat{\mathbf{B}}^{\mathrm{dip}}(\mathbf{r}_q), \tag{H1}$$

where $\hat{\mathbf{S}}$ is a spin-1 operator of the NV-center, Δ_{NV} is its zero-field splitting, γ_q is its gyromagnetic ratio, and $\mathbf{B}^{\mathrm{dip}}(\mathbf{r}_q)$ is the dipole field produced by the magnet at the NV position [see Eq. (B5)]. In the following, as the derivation is the same at each node, we drop the site-index j.

Expressing the NV spin operators in terms of the eigenstates of $\hat{S}_z$, namely $\hat{S}_z = |1\rangle\langle 1| - |-1\rangle\langle -1|$ and $\hat{S}_+ = (\hat{S}_-)^{\dagger} = \sqrt{2}(|0\rangle\langle -1| + |1\rangle\langle 0|)$, the Hamiltonian Eq. (H1) can be rewritten as $\hat{H}_{\text{M-NV}} = \hat{H}_1 + \hat{H}_{-1}$, where $\hat{H}_k$ acts only on the

states $|0\rangle, |k\rangle$ $(k = \pm 1)$ of the NV center. In the following, we assume the frequency of the magnon to be close to the NV center transition frequency between $|0\rangle$ and $|-1\rangle$. This can be achieved by appropriate values of the applied field B_0, the magnet size R, and the relative distance r_q between the NV and the magnet [see Fig. 3(c)]. With this assumption, the coupling between the magnet and the higher level $|1\rangle$ is negligible, and the NV-magnet coupling is thus well approximated by $\hat{H}_{-1}$. Hence, within the two-level approximation and the Holstein-Primakoff approximation, the magnon-NV center Hamiltonian is given by

$$\begin{aligned}\hat{H}_{\rm MQ} &= \hbar\omega_\sigma(\theta)\frac{\hat{\sigma}^z}{2} + \hbar\frac{\sqrt{F}}{2}\xi(\theta)(e^{i\varphi}\hat{\sigma}^- + \text{H.c.}) \\ &\quad - \hbar\{[g(\theta)e^{-i2\varphi}\hat{f}^\dagger + \Omega(\theta)\hat{f}]\hat{\sigma}^- + \text{H.c.}\} \\ &\quad + \hbar\xi(\theta)(e^{i\varphi}\hat{f} + \text{H.c.})\frac{\hat{\sigma}^z}{2},\end{aligned} \tag{H2}$$

where $\hat{\sigma}^z \equiv |-1\rangle\langle -1| - |0\rangle\langle 0|$, $\hat{\sigma}^+ = |-1\rangle\langle 0|$, $\hat{\sigma}^- \equiv |0\rangle\langle -1|$, and we defined the frequencies

$$\omega_\sigma(\theta) \equiv \Delta_{\rm NV} - \gamma_q B_0 - \frac{\hbar\gamma_0\gamma_q\mu_0}{4\pi r_q^3}F(3\cos^2\theta - 1), \tag{H3}$$

$$\xi(\theta) \equiv \frac{3\hbar\gamma_q\gamma_0\mu_0}{4\pi r_q^3}\sqrt{2F}\sin\theta\cos\theta, \tag{H4}$$

$$\Omega(\theta) \equiv \frac{\hbar\gamma_0\gamma_q\mu_0}{8\pi r_q^3}\sqrt{F}(3\sin^2\theta - 2), \tag{H5}$$

$$g(\theta) \equiv \frac{3\hbar\gamma_0\gamma_q\mu_0}{8\pi r_q^3}\sqrt{F}\sin^2\theta. \tag{H6}$$

The spin qubit in Eq. (H2) can be diagonalized in terms of dressed states $|\pm\rangle$. These are obtained from the uncoupled state $|0\rangle, |-1\rangle$ by the unitary transformation matrix

$$\hat{U} = \begin{pmatrix} e^{-i\varphi/2}\cos(\Theta/2) & -e^{-i\varphi/2}\sin(\Theta/2) \\ e^{i\varphi/2}\sin(\Theta/2) & e^{i\varphi/2}\cos(\Theta/2)\end{pmatrix}, \tag{H7}$$

where the angle $\Theta \in [0, \pi]$ is defined as

$$\Theta = \begin{cases} \pi - \arctan\left(\frac{\sqrt{F}|\xi(\theta)|}{|\omega_\sigma(\theta)|}\right), & \xi(\theta)/\omega_\sigma(\theta) < 0, \\ \arctan\left(\frac{\sqrt{F}|\xi(\theta)|}{|\omega_\sigma(\theta)|}\right), & \xi(\theta)/\omega_\sigma(\theta) > 0. \end{cases} \tag{H8}$$

In the dressed state basis, Eq. (H2) reads

$$\begin{aligned}\hat{H}_{\rm MQ} &= \hbar\omega_\sigma\frac{\hat{\sigma}^z}{2} + \hbar\xi(e^{i\varphi}\hat{f} + \text{H.c.})\frac{\hat{\sigma}^z}{2} \\ &\quad - \hbar g(e^{i\varphi}\hat{f}^\dagger|+\rangle\langle -| + \text{H.c.}) \\ &\quad - \hbar\Omega(e^{i\varphi}\hat{f}^\dagger|-\rangle\langle +| + \text{H.c.}).\end{aligned} \tag{H9}$$

The Pauli operator in Eq. (H9) refers now to the dressed states, namely $\hat{\sigma}^z \equiv |+\rangle\langle +| - |-\rangle\langle -|$. The dressed state frequency is

$$\omega_\sigma \equiv \sqrt{\omega_\sigma(\theta)^2 + F\xi(\theta)^2}, \tag{H10}$$

and the spin qubit-magnon couplings are

$$\xi \equiv \xi(\theta)e^{i\varphi}\cos\Theta + (\Omega(\theta)e^{-i\varphi} + g(\theta)e^{2i\varphi})\sin\Theta, \tag{H11}$$

$$g \equiv \tfrac{1}{4}\xi(\theta)\sin\Theta + g(\theta)\cos^2(\Theta/2) - \Omega(\theta)\sin^2(\Theta/2), \tag{H12}$$

and

$$\Omega \equiv \tfrac{1}{4}\xi(\theta)\sin\Theta + \Omega(\theta)\cos(\Theta/2) - g(\theta)\sin(\Theta/2). \tag{H13}$$

Figure 7 shows the dependence of the coupling ξ, g, and Ω in Eqs. (H11), (H12), and (H13) as a function of θ.

The Hamiltonian describing the general scenario of quantum emitters (NV centers) locally coupled to the magnets in a HML by magnetic dipole-dipole interaction reads $\hat{H}_{\rm T} = \hat{H}_{\rm M} + \sum_{j=1}^{N}\hat{H}_{\rm MQ}^j$, where $\hat{H}_{\rm M}$ is the Hamiltonian of the HML and $\hat{H}_{\rm MQ}^j$ is the magnet-NV interaction at site j and is given by Eq. (H9). For a quasiresonant interaction, $\Delta \equiv \omega_0 - \omega_\sigma \ll \omega_\sigma, \omega_0$, the total Hamiltonian of the system, within the rotating-wave approximation, is given by the following Jaynes-Cummings-Hubbard Hamiltonian:

$$\begin{aligned}\hat{H}_{\rm T} &= \hbar\sum_{\mathbf{j}}\left[\omega_0\hat{f}_{\mathbf{j}}^\dagger\hat{f}_{\mathbf{j}} + \omega_\sigma\frac{\hat{\sigma}_{\mathbf{j}}^z}{2} - g(\hat{f}_{\mathbf{j}}^\dagger\hat{\sigma}_{\mathbf{j}}^- + \hat{f}_{\mathbf{j}}\hat{\sigma}_{\mathbf{j}}^+)\right] \\ &\quad + \hbar\mathcal{J}\sum_{\mathbf{i}\neq\mathbf{j}}\hat{f}_{\mathbf{i}}\hat{f}_{\mathbf{j}}^\dagger,\end{aligned} \tag{H14}$$

where $\mathbf{j} = (j_x, j_y)$ and $\mathbf{i} = (i_x, i_y)$ are the index labeling the nodes of a general 2D HML. Note that Eq. (H14) is the real-space representation of Eq. (12) in the main text.

APPENDIX I: EFFECTIVE SPIN-SPIN INTERACTION THROUGH A MAGNONIC QUANTUM BUS

In this Appendix, we derive Eq. (13) describing the magnon-mediated interaction between the two qubits, and we obtain the figure of merit presented in Sec. III C, which estimates the efficacy of a SWAP gate operation performed by the magnonic quantum bus.

We consider two spin qubits locally coupled by magnetic dipole-dipole interactions to two magnetic particles coupled by a superconducting loop resonator [see Fig. 3(a)]. The dynamics of the quantum state of the total system is described by the following master equation:

$$\begin{aligned}\partial_t\hat{\rho} &= -\frac{i}{\hbar}[\hat{H}_{\rm T}, \hat{\rho}] + \kappa\sum_{j=1}^{2}\left(\hat{f}_j\hat{\rho}\hat{f}_j^\dagger - \frac{1}{2}\{\hat{f}_j^\dagger\hat{f}_j, \hat{\rho}\}\right) \\ &\quad + \gamma\sum_{j=1}^{2}\left(\hat{\sigma}_j^z\hat{\rho}\hat{\sigma}_j^z - \hat{\rho}\right),\end{aligned} \tag{I1}$$

where $\hat{\rho}$ represents the quantum state of the two qubits and the magnons at site $j = 1, 2$, κ is the magnon damping rate, $\gamma \equiv \pi/T_2^*$ the qubit dephasing rate, and $\hat{H}_{\rm T}$ is defined in Eq. (H14) for the simple case in which $i, j = 1, 2$. In terms of the modes $\hat{f}_\pm \equiv (\hat{f}_1 \pm \hat{f}_2)/\sqrt{2}$, the Hamiltonian $\hat{H}_{\rm T}$ reads

$$\begin{aligned}\hat{H}_{\rm T} &= \hbar\omega_+\hat{f}_+^\dagger\hat{f}_+ + \hbar\omega_-\hat{f}_-^\dagger\hat{f}_- + \hbar\omega_\sigma\left(\frac{\hat{\sigma}_1^z}{2} + \frac{\hat{\sigma}_2^z}{2}\right) \\ &\quad - \frac{g}{\sqrt{2}}[\hat{f}_+(\hat{\sigma}_1^+ + \hat{\sigma}_2^+) + \hat{f}_-(\hat{\sigma}_1^+ - \hat{\sigma}_2^+) + \text{H.c.}],\end{aligned} \tag{I2}$$

where $\omega_\pm \equiv \omega_0 \pm \mathcal{J}$. The dissipative term in Eq. (I1) maintains the same structure whereas the magnonic operators $\hat{f}_j, \hat{f}_j^\dagger$ $(j = 1, 2)$ are replaced by the normal modes $\hat{f}_\pm^\dagger, \hat{f}_\pm$.

In the limit of a large detuning between the spin qubits and the magnons, it is possible to adiabatically eliminate the magnonic degrees of freedom and obtain an effective master equation describing the effective dynamics of the spin qubits. Transforming the master equation describing the total system via the unitary operator

$$\hat{U} \equiv \exp\left\{-\frac{g}{\sqrt{2}\Delta}[\hat{f}_+^\dagger(\hat{\sigma}_1^- + \hat{\sigma}_2^-) - \text{H.c.}] - \frac{g}{\sqrt{2}(\Delta - 2\mathcal{J})}[\hat{f}_-^\dagger(\hat{\sigma}_1^- - \hat{\sigma}_2^-) - \text{H.c.}]\right\}, \quad \text{(I3)}$$

keeping terms up to second order in g/Δ, $g/(\Delta - 2\mathcal{J}) \ll 1$, and projecting the result on the vacuum subspace of the magnons Hilbert space, one obtains

$$\partial_t \hat{\rho}_{\text{eff}} = -\frac{i}{\hbar}[\hat{H}_{\text{QQ}}, \hat{\rho}_{\text{eff}}] + \kappa_{\text{eff}} \sum_{j=1}^{2} \mathcal{D}^{jj}_{\hat{\sigma}^-}[\hat{\rho}_{\text{eff}}] + \Omega_{\text{eff}} \sum_{i\neq j=1}^{2} \mathcal{D}^{ij}_{\hat{\sigma}^-}[\hat{\rho}_{\text{eff}}] + \gamma \sum_{j=1}^{2} \left(\hat{\sigma}_j^z \hat{\rho} \hat{\sigma}_j^z - \hat{\rho}\right), \quad \text{(I4)}$$

where

$$\hat{H}_{\text{QQ}} \equiv \frac{\hbar}{2}\tilde{\omega}_\sigma\left(\hat{\sigma}_1^z + \hat{\sigma}_2^z\right) - \hbar g_{\text{eff}}(\hat{\sigma}_1^+ \hat{\sigma}_2^- + \hat{\sigma}_1^- \hat{\sigma}_2^+), \quad \text{(I5)}$$

and

$$\mathcal{D}^{ij}_{\hat{\sigma}^-}[\hat{\rho}_{\text{eff}}] \equiv \hat{\sigma}_i^- \hat{\rho}_{\text{eff}} \hat{\sigma}_j^+ - \tfrac{1}{2}\{\hat{\sigma}_j^+ \hat{\sigma}_i^-, \hat{\rho}_{\text{eff}}\}. \quad \text{(I6)}$$

Here, $\hat{\rho}_{\text{eff}}$ represents the effective state of the two qubits, and we defined the effective frequencies and decay rates

$$\tilde{\omega}_\sigma \equiv \omega_\sigma - g^2\left(\frac{1}{\Delta - 2\mathcal{J}} + \frac{1}{\Delta}\right), \quad \text{(I7)}$$

$$g_{\text{eff}} \equiv g^2\left(\frac{1}{\Delta} - \frac{1}{\Delta - 2\mathcal{J}}\right), \quad \text{(I8)}$$

$$\kappa_{\text{eff}} \equiv \kappa\, g^2 \frac{\Delta^2 + (\Delta - 2\mathcal{J})^2}{\Delta^2(\Delta - 2\mathcal{J})^2}, \quad \text{(I9)}$$

$$\Omega_{\text{eff}} \equiv \kappa\, g^2 \frac{\Delta^2 - (\Delta - 2\mathcal{J})^2}{\Delta^2(\Delta - 2\mathcal{J})^2}. \quad \text{(I10)}$$

The Hamiltonian Eq. (I5) can be used to implement a long-range qubit-qubit interaction through the magnonic quantum bus provided by a HML.

The intrinsic qubit dephasing γ as well as the bus-induced effective qubit damping κ_{eff} described in Eq. (I4) affect the performance of coherent exchange of excitations between the qubits. In the following, we describe the impact of these noise sources and derive a figure of merit for the performance of the coherent qubit coupling.

Let us consider a SWAP gate that transfers an excitation from the first to the second qubit through the interaction described by Eq. (I5). The performance of the gate can be estimated in terms of the quantum state fidelity [71] $\mathcal{F}(t) = [\text{Tr}\sqrt{\langle\psi_t|\hat{\rho}(t)|\psi_t\rangle}]^2$ between the state of the system $\hat{\rho}(t)$ after the evolution governed by Eq. (I1) and the target state $|\psi_t\rangle \equiv |01\rangle \otimes |\text{vac}\rangle$, where $|\text{vac}\rangle$ is the vacuum of the magnon bus and $|01\rangle$ is the two qubits state where only the second (target) qubit is excited. We assume that the system is initially prepared in the pure state $\hat{\rho}(0) = |\psi\rangle\langle\psi|$ with $|\psi\rangle \equiv |10\rangle \otimes |\text{vac}\rangle$, where only the first qubit is excited. The performance of the SWAP gate can then be estimated by maximizing $\mathcal{F}(t)$ over the total evolution time t, and calculating the fidelity error $\varepsilon \equiv 1 - \max_t[\mathcal{F}(t)]$ in the presence of noise. A numerical optimization of ε over all the relevant parameters of the system g, $\mathcal{J}$, Δ, κ, and γ yields a figure of merit for the performance of the gate.

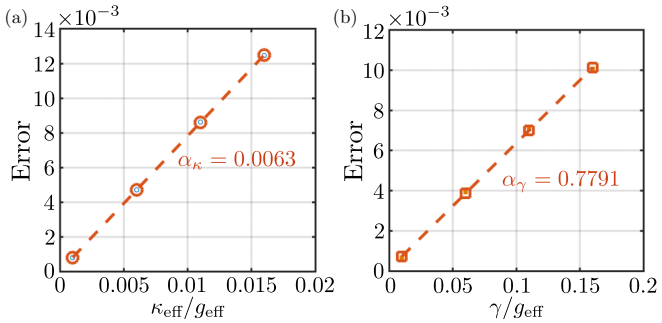

FIG. 8. Distribution of the fidelity error ε for the optimized detuning $\Delta^* = \mathcal{J}$ as a function of (a) κ/g_{eff} for $\pi/T_2^* = 0$ and (b) γ/g_{eff} for $\kappa = 0$. Each panel shows the numerically calculated points (square/circles) together with the linear interpolation (dashed line) with slope (a) α_κ and (b) α_γ.

An analytical expression for the scaling of the optimal error can be obtained in the dispersive regime g/Δ, $g/(\Delta - 2\mathcal{J}) \ll 1$. In the strong-coupling limit $g_{\text{eff}} \gg \kappa_{\text{eff}}, \gamma, \varepsilon$ scales approximately linearly with the decoherence rates as $\varepsilon \approx \alpha_\gamma \gamma/g_{\text{eff}} + \alpha_\kappa \kappa_{\text{eff}}/g_{\text{eff}}$ [72], where the coefficients α_γ and α_κ are assumed to be approximately independent of the detuning Δ. This assumption can be numerically checked by simulating the error scaling for different values of Δ for the same values of $\kappa_{\text{eff}}/g_{\text{eff}}, \gamma/g_{\text{eff}} \ll 1$. After substituting Eq. (I8) into the linear expansion for ε, one obtains

$$\varepsilon = -\alpha_\gamma \frac{\gamma\Delta(\Delta - 2\mathcal{J})}{2g^2\mathcal{J}} - \alpha_\kappa \frac{\kappa}{2}\frac{\Delta^2 + (\Delta - 2\mathcal{J})}{\mathcal{J}\Delta(\Delta - 2\mathcal{J})}. \quad \text{(I11)}$$

For the optimal values $\Delta^* = \mathcal{J}^* = \sqrt{2\alpha_\kappa g^2 \kappa T_2^*/(\pi\alpha_\gamma)}$ [73], Eq. (I11) reads

$$\varepsilon = \sqrt{\frac{\alpha_\kappa \alpha_\gamma}{2C_0}}, \quad \text{(I12)}$$

where the cooperativity C is defined as

$$C_0 = \frac{g^2}{\gamma\kappa}. \quad \text{(I13)}$$

In Fig. 8, the error ε optimized for $\Delta = \mathcal{J}$ is plotted as a function of the normalized decoherence rates $\kappa_{\text{eff}}/g_{\text{eff}}$ and γ/g_{eff}.

[1] C. Kittel, *Quantum Theory of Solids* (Wiley, New York, 1987).

[2] A. L. Fetter and J. D. Walecka, *Quantum Theory of Many-particle Systems* (Dover Publications Inc., New York, 2003).

[3] J. D. Joannopoulos, S. G. Johnson, J. N. Winn, and R. D. Meade, *Photonic Crystals: Molding the Flow of Light* (Princeton University Press, Princeton, NJ, 2011).

[4] D. E. Chang, J. S. Douglas, A. González-Tudela, C.-L. Hung, and H. J. Kimble, Rev. Mod. Phys. **90**, 031002 (2018).

[5] J. S. Douglas, H. Habibian, C. L. Hung, A. V. Gorshkov, H. J. Kimble, and D. E. Chang, Nat. Photon. **9**, 326 (2015).

[6] J. D. Hood, A. Goban, A. Asenjo-Garcia, M. Lu, S.-P. Yu, D. E. Chang, and H. J. Kimble, Proc. Natl. Acad. Sci. **113**, 10507 (2016).

[7] C.-L. Hung, A. González-Tudela, J. I. Cirac, and H. J. Kimble, Proc. Natl. Acad. Sci. USA **113**, E4946 (2016).

[8] M. J. A. Schuetz, J. Knörzer, G. Giedke, L. M. K. Vandersypen, M. D. Lukin, and J. I. Cirac, Phys. Rev. X **7**, 041019 (2017).

[9] M. J. A. Schuetz, E. M. Kessler, G. Giedke, L. M. K. Vandersypen, M. D. Lukin, and J. I. Cirac, Phys. Rev. X **5**, 031031 (2015).

[10] N. Y. Yao, L. Jiang, A. V. Gorshkov, P. C. Maurer, G. Giedke, J. I. Cirac, and M. D. Lukin, Nat. Commun. **3**, 800 (2012).

[11] R. Manenti, A. F. Kockum, A. Patterson, T. Behrle, J. Rahamim, G. Tancredi, F. Nori, and P. J. Leek, Nat. Commun. **8**, 975 (2017).

[12] A. González-Tudela and J. I. Cirac, Phys. Rev. A **96**, 043811 (2017).

[13] S. John and T. Quang, Phys. Rev. A **50**, 1764 (1994).

[14] H. Huebl, C. W. Zollitsch, J. Lotze, F. Hocke, M. Greifenstein, A. Marx, R. Gross, and S. T. B. Goennenwein, Phys. Rev. Lett. **111**, 127003 (2013).

[15] Y. Tabuchi, S. Ishino, T. Ishikawa, R. Yamazaki, K. Usami, and Y. Nakamura, Phys. Rev. Lett. **113**, 083603 (2014).

[16] N. J. Lambert, J. A. Haigh, S. Langenfeld, A. C. Doherty, and A. J. Ferguson, Phys. Rev. A **93**, 021803(R) (2016).

[17] X. Zhang, C. Zou, L. Jiang, and H. X. Tang, J. Appl. Phys. **119**, 023905 (2016).

[18] D. Zhang, X.-M. Wang, T.-F. Li, X.-Q. Luo, W. Wu, F. Nori, and J. You, npj Quantum Inf. **1**, 15014 (2015).

[19] B. Zare Rameshti, Y. Cao, and G. E. W. Bauer, Phys. Rev. B **91**, 214430 (2015).

[20] O. O. Soykal and M. E. Flatté, Phys. Rev. Lett. **104**, 077202 (2010).

[21] S. Viola Kusminskiy, H. X. Tang, and F. Marquardt, Phys. Rev. A **94**, 033821 (2016).

[22] A. Osada, R. Hisatomi, A. Noguchi, Y. Tabuchi, R. Yamazaki, K. Usami, M. Sadgrove, R. Yalla, M. Nomura, and Y. Nakamura, Phys. Rev. Lett. **116**, 223601 (2016).

[23] J. A. Haigh, N. J. Lambert, S. Sharma, Y. M. Blanter, G. E. W. Bauer, and A. J. Ramsay, Phys. Rev. B **97**, 214423 (2018).

[24] Y. Tabuchi, S. Ishino, A. Noguchi, T. Ishikawa, R. Yamazaki, K. Usami, and Y. Nakamura, Science **349**, 405 (2015).

[25] Y. Tabuchi, S. Ishino, A. Noguchi, T. Ishikawa, R. Yamazaki, K. Usami, and Y. Nakamura, C. R. Phys. **17**, 729 (2016).

[26] S. Nikitov, P. Tailhades, and C. Tsai, J. Magn. Magn. Mater. **236**, 320 (2001).

[27] M. Krawczyk and D. Grundler, J. Phys.: Condens. Matter **26**, 123202 (2014).

[28] A. Chumak, A. Serga, and B. Hillebrands, J. Phys. D **50**, 244001 (2017).

[29] P. Andrich, C. F. de las Casas, X. Liu, H. L. Bretscher, J. R. Berman, F. J. Heremans, P. F. Nealey, and D. D. Awschalom, npj Quantum Inf. **3**, 28 (2017).

[30] S. Kosen, R. G. E. Morris, A. F. van Loo, and A. D. Karenowska, Appl. Phys. Lett. **112**, 012402 (2018).

[31] L. Trifunovic, F. L. Pedrocchi, and D. Loss, Phys. Rev. X **3**, 041023 (2013).

[32] H. Qin, G.-J. Both, S. J. Hämäläinen, L. Yao, and S. van Dijken, Nat. Commun. **9**, 5445 (2018).

[33] J. Topp, D. Heitmann, M. P. Kostylev, and D. Grundler, Phys. Rev. Lett. **104**, 207205 (2010).

[34] G. Gubbiotti, S. Tacchi, G. Carlotti, N. Singh, S. Goolaup, A. O. Adeyeye, and M. Kostylev, Appl. Phys. Lett. **90**, 092503 (2007).

[35] D. Davidović, S. Kumar, D. H. Reich, J. Siegel, S. B. Field, R. C. Tiberio, R. Hey, and K. Ploog, Phys. Rev. Lett. **76**, 815 (1996).

[36] U. Vool and M. Devoret, Int. J. Circ. Theor. Appl. **45**, 897 (2017).

[37] D. De Bernardis, T. Jaako, and P. Rabl, Phys. Rev. A **97**, 043820 (2018).

[38] S. Chikazumi and C. D. Graham, *Physics of Ferromagnetism 2e* (Oxford University Press on Demand, Oxford, UK, 2009).

[39] We define the spin operator to be dimensionless, namely $[\hat{F}_i, \hat{F}_j] = i\epsilon_{ijk}\hat{F}_k$.

[40] With this configuration, the field intensity at the surface of the coil generated by the magnet is $B \approx 50$ mT (Appendix E). Depending on the distance between the particle and the loop, it might be necessary to consider the loop to be made of a high-T_c superconductor (see Appendix E).

[41] M. Gross and S. Haroche, Phys. Rep. **93**, 301 (1982).

[42] G. Grosso and G. Pastori Parravicini, *Solid State Physics* (Elsevier Science Publishing Co Inc., San Diego, 2013).

[43] A. González-Tudela and J. I. Cirac, Phys. Rev. Lett. **119**, 143602 (2017).

[44] A. Gruber, A. Dräbenstedt, C. Tietz, L. Fleury, J. Wrachtrup, and C. v. Borczyskowski, Science **276**, 2012 (1997).

[45] D. G. Angelakis, M. F. Santos, and S. Bose, Phys. Rev. A **76**, 031805(R) (2007).

[46] A. D. Greentree, C. Tahan, J. H. Cole, and L. C. L. Hollenberg, Nat. Phys. **2**, 856 (2006).

[47] N. Zhao, J. Honert, B. Schmid, M. Klas, J. Isoya, M. Markham, D. Twitchen, F. Jelezko, R.-B. Liu, H. Fedder, and J. Wrachtrup, Nat. Nanotechnol. **7**, 657 (2012).

[48] M. H. Abobeih, J. Cramer, M. A. Bakker, N. Kalb, M. Markham, D. J. Twitchen, and T. H. Taminiau, Nat. Commun. **9**, 2552 (2018).

[49] I. Boventer, M. Pfirrmann, J. Krause, Y. Schön, M. Kläui, and M. Weides, Phys. Rev. B **97**, 184420 (2018).

[50] S. Klingler, H. Maier-Flaig, C. Dubs, O. Surzhenko, R. Gross, H. Huebl, S. T. B. Goennenwein, and M. Weiler, Appl. Phys. Lett. **110**, 092409 (2017).

[51] D. D. Stancil and A. Prabhakar, *Spin Waves* (Springer, New York, 2009).

[52] We remark that the effective description in Eq. (13) breaks down when the qubit is resonant with the magnonic modes, i.e., for

$\Delta \simeq 0, 2\mathcal{J}$ [see also Fig. 3(b)]. In this case, the dynamics of the system is correctly described by a master equation for the total magnons-qubit system (see Appendix I for details).

[53] C. Nisoli, R. Moessner, and P. Schiffer, Rev. Mod. Phys. **85**, 1473 (2013).

[54] L. J. Heyderman and R. L. Stamps, J. Phys.: Condens. Matter **25**, 363201 (2013).

[55] X. S. Ling, H. J. Lezec, M. J. Higgins, J. S. Tsai, J. Fujita, H. Numata, Y. Nakamura, Y. Ochiai, C. Tang, P. M. Chaikin, and S. Bhattacharya, Phys. Rev. Lett. **76**, 2989 (1996).

[56] J. Berger and J. Rubinstein, *Connectivity and Superconductivity* (Springer Science & Business Media, Berlin, Germany, 2001).

[57] J. Prat-Camps, C. Teo, C. C. Rusconi, W. Wieczorek, and O. Romero-Isart, Phys. Rev. Appl. **8**, 034002 (2017).

[58] C. C. Rusconi, V. Pöchhacker, K. Kustura, J. I. Cirac, and O. Romero-Isart, Phys. Rev. Lett. **119**, 167202 (2017).

[59] M. Goryachev, W. G. Farr, D. L. Creedon, Y. Fan, M. Kostylev, and M. E. Tobar, Phys. Rev. Appl. **2**, 054002 (2014).

[60] K. Chang and L.-H. Hsieh, *Microwave Ring Circuits and Related Structures* (John Wiley & Sons, New York, 2004).

[61] R. Hopkins and C. Free, IET Microwaves Antennas Propag. **2**, 66 (2008).

[62] Z. K. Minev, I. M. Pop, and M. H. Devoret, Appl. Phys. Lett. **103**, 142604 (2013).

[63] Z. K. Minev, K. Serniak, I. M. Pop, Z. Leghtas, K. Sliwa, M. Hatridge, L. Frunzio, R. J. Schoelkopf, and M. H. Devoret, Phys. Rev. Appl. **5**, 044021 (2016).

[64] H. Paik, D. I. Schuster, L. S. Bishop, G. Kirchmair, G. Catelani, A. P. Sears, B. R. Johnson, M. J. Reagor, L. Frunzio, L. I. Glazman, S. M. Girvin, M. H. Devoret, and R. J. Schoelkopf, Phys. Rev. Lett. **107**, 240501 (2011).

[65] F. W. Grover, *Inductance Calculations: Working Formulas and Tables* (Dover Publications Inc., New York, 2009).

[66] Without loss of generality, we assumed no flux trapped in the loop at the initial time.

[67] J. Miltat, G. Albuquerque, and A. Thiaville, in *Spin Dynamics in Confined Magnetic Structures I* (Springer, Berlin, Germany, 2002), pp. 1–33.

[68] J. D. Jackson, *Classical Electrodynamics* (John Wiley & Sons, New York, 1998).

[69] For the elementary two-magnet configuration in Fig. 1(b), $\theta_{12} = 0$, $\varphi_{ij} = \pi/2$, thus the first term in Eq. (D8) cancels.

[70] B. W. Roberts, J. Phys. Chem. Ref. Data **5**, 581 (1976).

[71] R. Jozsa, J. Mod. Opt. **41**, 2315 (1994).

[72] M. J. A. Schuetz, G. Giedke, L. M. K. Vandersypen, and J. I. Cirac, Phys. Rev. A **95**, 052335 (2017).

[73] Different solutions for $d\varepsilon/d\Delta = 0$ are possible, however only $\Delta = \mathcal{J}$ satisfies the condition $g/\mathcal{J} \ll 1$ for the dispersive regime.